Process optimization of Gas Metal Arc Brazing technology

by

Yong Hwan Cho

A thesis

presented to the University of Waterloo

in fulfillment of the

thesis requirement for the degree of

Master of Applied Science

in

Mechanical and Mechatronics Engineering

Waterloo, Ontario, Canada, 2022

Author’s Declaration

This thesis consists of material all of which I authored or co-authored: see Statement of contributions included in the thesis. This is a true copy of the thesis, including any required final revisions, as accepted by my examiners.

I understand that my thesis may be made electronically available to the public.

Statement of Contributions

This thesis was solely written by the candidate. Professor N. Zhou and M. Shehryar Khan contributed to the editing of this thesis.

Chapter 4 of this thesis is based on the journal paper which has been published in *The International Journal of Advanced Manufacturing Technology*:

> Yong Hwan Cho, Shehryar Khan, M., Goodwin, F.E. *et al.* Effect of torch angle and position on bead geometry and joint strength during arc brazing of thin-gauge dual-phase steel. *Int J Adv Manuf Technol* 121, 543–557 (2022). https://doi.org/10.1007/s00170-022-09309-7

The experiment, data collection, and analysis were performed by the candidate with support from M. Shehryar Khan. The paper was co-authored by the candidate, M. Shehryar Khan, F.E. Goodwin, Y. N. Zhou. All figures in Chapter 4 are used with permission of Springer Nature BV; permission conveyed through Copyright Clearance Center, Inc.

Chapter 5 and 6 of this thesis is based on the results from a conference paper:

> Yong Hwan Cho, M. Shehryar Khan, B. Klassen, Y. Zhou, "Influence of surface treatment on joint strength during MIG brazing of GI and GA coated DP600." Sheet Metal Welding Conference XIX, 2021

The experiment, analysis, and writing were conducted by the candidate with support from M. Shehryar Khan. The paper was co-authored by the candidate, M. Shehryar Khan, B. Klassen, Y.N. Zhou. Data collection was conducted by the candidate and support from B. Klassen who was a co-op student. The first draft of the manuscript was written by the candidate and subsequently improved by M. Shehryar Khan. The data used for the creation of DIC image (Figure 5.3a and Figure 5.10b) and elemental map (Figure 6.2) were obtained by M. Shehryar Khan.

Abstract

Gas-metal-arc brazing (GMAB) technology is a transformative non-fusion joining process used in the joining of thin-gauge Zn-coated advanced high strength steels (AHSSs) employed in the automotive industry. Due to its lower heat input capability, the technology offers several benefits over the conventional gas-metal-arc welding (GMAW) process such as minimal Zn-coating burn-off, lower distortion, minimal welding defects, and a reduced heat-affected-zone (HAZ), which make GMAB more suitable for joining thin-gauge galvanized AHSSs.

Being a relatively new technology compared to other conventional welding processes, the process technology of GMAB is yet to be fully optimized based on the existing literature. In this thesis, three factors of the process variables that were found to be critically influential on the mechanical properties of GMA brazed lap joint were investigated to further optimize GMAB process technology; the three factors are the torch angle and position, the gap clearance, and the Zn-coating type.

The results showed that the torch parameters have a large influence on the behavior of arc and droplet transfer which have a direct impact on the bead geometry, heat distribution, and joint strength. The mechanical properties of the joint improved with the increase of torch angles and centering of the torch position at the root region.

The effect of gap clearance has not been considered a factor of influence during the GMAB process as the capillary action does not play a role in the GMAB process. However, results showed that the presence of a gap and proper wetting of filler material through the gap greatly reduced the stress concentration developing at the root region due to the bending of base metal sheets driven by the eccentricity of load during the lap-shear tensile test. It was shown that the use of a gap size between 0.3–0.6 mm resulted in the optimal joint strength.

The chemistry of zinc coating type (GI and GA) was shown to have a critical influence on the mechanical properties of the joint due to the formation of Cu-Zn alloy at the tail-end area of the root region. GI-coating had a detrimental effect on the joint strength due to the

formation of extremely brittle zinc-rich-area in the root region which is highly susceptible to crack formation. On the other hand, GA-coated samples had superior joint strength in general due to the formation of a much more ductile zinc-rich area in the root region.

Acknowledgements

Foremost, I would like to thank my supervisor, Prof. Norman Zhou for giving me the opportunity to do research and providing all the guidance and support throughout my master's study. It was truly the most invaluable learning experience of my academic career.

Secondly, I would like to express special thanks to M. Shehryar Khan for being my mentor, advisor, and friend throughout my master's study. I was very fortunate to have him as my research partner and work together on every step of the project.

I would also like to express my gratitude to the industry partners International Zinc Association (IZA) and the Galvanized Autobody Partnership for supporting this project.

Special thanks to Dr. Erika Bellhouse at ArcelorMittal Dofasco for the in-kind support by supplying the base materials used in this study.

Another special thanks to the team at Lincoln Electric (Tim Hurley, Vivek Sengupta, and Vladimir Yasnogorodski) for the in-kind support by supplying the Si-Bronze filler material and providing access to their research facilities.

Lastly, I would like to thank my colleagues in CAMJ for all their support and encouragement over the past two years.

Table of Contents

List of Figures

List of Tables

List of Abbreviations

AHSS	Advanced high strength steel
AR	As-received
BB	Braze bead
BM	Base metal
CCT	Continuous cooling transformation
CGHAZ	Coarse-grained HAZ
DIC	Digital image correlation
DOE	Design of experiment
DP	Dual-phase
FGHAZ	Fine-grained HAZ
GA	Hot-dip galvannealed
GI	Hot-dip galvanized
GMAB	Gas metal arc brazing
GMAW	Gas metal arc welding
HAZ	Heat-affected-zone
HSLA	High strength low alloy
IF	Interfacial
IMC	Intermetallic compound
OM	Optical microscopy
PCB	Plasma cleaned bottom
PCT	Plasma cleaned top
PCTB	Plasma cleaned top and bottom
PMZ	Partial-melted-zone
TP	torch position
TS	Travel speed
UTS	Ultimate tensile strength
VI	Vertical interface
WFS	Wire feed speed
ZRA	Zinc-rich area

List of Symbols

α	Work angle
β	Push angle
H	Bead height
S	Throat length
θ	Toe angle
W	Bead width
G	Gap size
L_1	Leg length
L_2	Wetting length of the bottom interface
L_3	Root wetting length at the top sheet
L_4	Root wetting length at bottom sheet
PMZ_1	Partial melted zone at the top sheet
PMZ_2	Partial melted zone at the bottom sheet

Chapter 1
Introduction

In past decades, lightweight vehicle design has been the key factor to improve vehicle performance and fuel efficiency. This is achieved by using thin-gauge advanced high strength steels (AHSS) in the production of structural components that make up the body-in-white frame of modern vehicles. These components offer the desired combination of strength, ductility, toughness, and fatigue resistance, which allows the reduction of material thickness while maintaining structural integrity for improved safety [1]. AHSSs are known to have poor corrosion resistance and are commonly coated with various types of coatings (i.e. Al-Si, Zn, Zn-Al-Mg, etc.) to offer some type of barrier or sacrificial protection. However, it is also widely known that these coatings tend to be problematic during the welding of these steels [2–9]. Despite these known issues, it would be impossible to provide an acceptable service life to a vehicle made from AHSSs without these coatings. Zn-coatings are the most typically used protection method against corrosion for AHSS due to their excellent ability to provide barrier protection, as well as sacrificial protection [10–12].

However, Zn-coatings have inherent problems associated with weldability using conventional fusion joining methods [2,5,13,14]. Due to the low melting point (420°C) and boiling point (907°C) of zinc, the coating tends to evaporate violently due to the high heat input (HI) associated with conventional welding methods, i.e., Gas Metal Arc Welding (GMAW), which causes problems such as porosity, blowholes, and zinc burn-off around the joint that makes it vulnerable to corrosion. More recently, Zn-coatings have been shown to play a significant role in liquid metal embrittlement (LME) cracking observed in fusion welds made using different processes [14–18]. Due to these issues associated with the fusion joining of Zn-coated steels, there has been a push to investigate non-fusion joining processes such as adhesive bonding [19–21] and weld-brazing [22,23] which is a technique that uses traditional welding heat sources, such as arc and laser, to melt low melting temperature filler materials which are then applied as a braze to join the substrates without melting them.

Gas-metal-arc-brazing (GMAB or GMA brazing) is a non-fusion joining method derived from the conventional GMAW process. By using low melting point filler wires and lower power input, the GMAB process is more suitable for joining thin-gauge Zn-coated AHSS compared to the GMAW process [24]. There are three main advantages of GMAB over GMAW process:

1. Conventional arc welding of thin gauge galvanized steel is known to cause a detrimental effect on weld quality such as porosity and blowholes due to the severe vaporization of Zn-coating that has a boiling point of 904°C [24]. Moreover, the high heat input from the welding process causes zinc burn-off near the joint leaving the steel substrate vulnerable to corrosion [25]. Such zinc burn-off is significantly reduced for the GMAB process and zinc coating is able to provide galvanic protection even within 1–2mm near the region where the coating has been lost. In addition, the lower process temperature of the GMAB process reduces the welding defects caused by the vaporization of zinc coating [24,26].
2. GMAB process offers lower heat input due to the lower melting temperature filler wires that require lower power input compared to the GMAW process, and subsequently, the thermal stresses caused by material expansion during the GMAB process are reduced. As a result, distortion of the parts is minimized compared to the conventional GMAW process [24,26].
3. The heat-affected zone (HAZ) softening phenomenon, which is the common welding defect for AHSSs caused by the tempering of the base metal microstructure within the HAZ region, is inherently reduced by the lower heat input of the GMAB process [13,27,28].

Being a relatively new technology compared to the other conventional welding processes, the GMAB process is yet to be fully optimized based on the existing literature. To further optimize the GMAB process, this thesis investigates critically influencing factors that affect the mechanical integrity of the GMA brazed lap joint.

1.1 Objective

The objective of this thesis is to optimize the GMAB process for the mechanical property of lap joint by investigating the fundamental effect of the following three key factors in the GMAB process for the mechanical properties in lap joint configuration.

- The torch angle and position
- The gap clearance of lap joint
- The zinc coating type.

1.2 Thesis outline

This thesis has been organized into seven chapters as outlined below:

Chapter 1 (Introduction) – Introduces the background and motivation for the development of the GMAB process and the objective of this thesis.

Chapter 2 (Literature Review) – Summarizes the fundamentals of the GMAB process based on existing literature. In addition, literature relevant to each topic in Chapters 4, 5, and 6 is discussed.

Chapter 3 (Methodology) – The details of the material, experiment, and equipment used for the experimental work performed for this thesis is stated.

Chapter 4 (Effect of torch angle and position) – The effect of torch position and angles on the location of droplet transfer, the behavior of arc, resulting bead geometry, and the mechanical properties of lap joints have been investigated.

Chapter 5 (Effect of gap clearance) – The effect of gap clearance and the wetting at the root region on the mechanical properties of GMA brazed lap joint has been investigated.

Chapter 6 (Effect of zinc-coating type) – The effect of Zn-coating type on microstructure and mechanical properties of GMA brazed lap joint has been investigated.

Chapter 7 (Conclusion) – Summarizes the main findings and conclusion from each main topic and proposes future work.

Chapter 2

Literature review

To further develop and optimize the GMAB process technology used for automotive applications, it is important to understand its background and state-of-the-art. In this chapter, the motivation that led to the invention and development of GMAB process technology is explained, and existing literature on the fundamentals of GMAB process technology is introduced. In addition, the literature review done for each topic in Chapters 4, 5, and 6 is discussed.

2.1 Advanced high strength steel (AHSS) in automotive

Until the 1970s, mild steels were the most popular choice for a steel sheet component of an automobile because it offers excellent formability and repairability which were the main design criteria at the time [1]. However, the worldwide oil crisis that broke out in 1973 resulted in an economic crisis and ever-growing environmental concerns, and changed the main driving factors for automotive design to minimization of energy consumption rate, or in another word, fuel efficiency [1]. Automotive manufacturers achieved this goal by reducing vehicular weight by changing the steel sheet components of cars from mild steel to advanced high strength steel (AHSS). AHSS have superior mechanical properties over conventional mild steel due to its carefully engineered microstructure and alloying elements that provide a wide range of strength, ductility, toughness, and fatigue property [29]. In general, the use of the appropriate type of AHSS reduces a vehicular weight by about 50% compared to using mild steel due to superior strength to ductility ratio which allows for halving thickness of sheet steel without sacrificing structural integrity and safety performance [1].

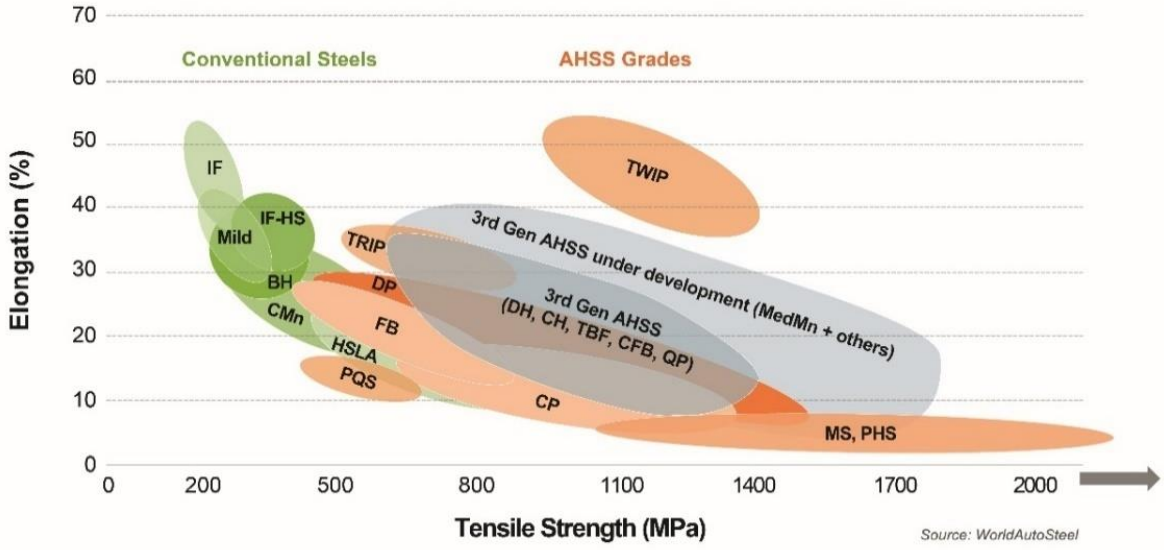

Figure 2.1 Steel strength-ductility diagram for today's AHSS Grades. Obtained from [30]**.**

2.2 Zn-coating

Like most steels, AHSS requires protection against corrosion. Zn-coating is commonly applied to AHSS during manufacturing to provide barrier protection to the steel, as well as cathodic protection even when the coating is scratched or damaged due to its lower electrode potential than iron [11,31]. In addition, Zn-coatings have great formability and paintability which is especially important factors for the manufacturing of cars [32]. Among the different types of Zn-coating available in the industry, hot-dipped galvanized (GI) coating is most commonly used for its ease of manufacturing that comes with excellent properties like strength, formability, and corrosion resistance [10,11]. As shown in Figure 2.2, the hot-dip galvanizing process can be incorporated into the continuous production line of a steel manufacturing process where the steel is dipped into a molten zinc bath of minimum 98% purity [11]. When a steel sheet is submerged in the molten zinc, zinc-iron multiphase intermetallic compound (IMC) layers are formed on the steel substrate with 100% pure zinc

at the outer top layer [11]. GI-coated steel can be further heat-treated by an annealing process to produce a hot-dip galvannealed (GA) coating. GA-coating contains higher iron content in the coating which provides additional properties such as higher corrosion resistance, paintability, and weldability [11,32,33]. GI and GA-coated AHSS are the most commonly used in the automotive industry [34]. For this reason, GI and GA-coated DP600 steel sheets are used as the base metal for this work.

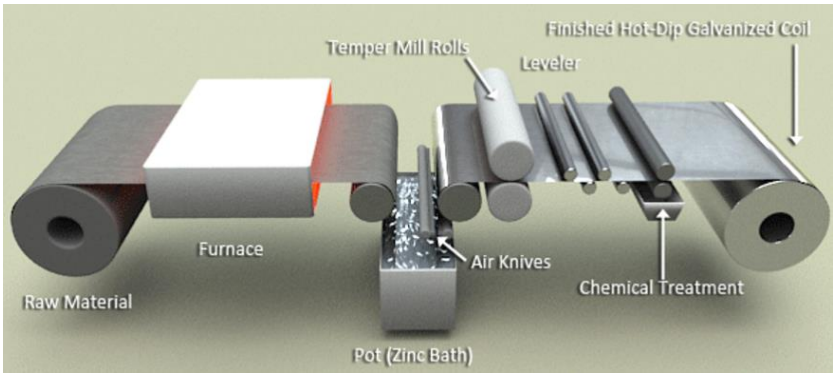

Figure 2.2: Hot-dip galvanizing process schematic. Obtained from [35]**.**

2.3 Gas metal arc brazing (GMAB)

GMAB is a non-fusion joining method developed for the joining of thin-gauge Zn-coated materials. The GMAB process is invented in the early 20th century and its first record can be found in the patent titled “Method for arc brazing using an inert gas” published on May 4, 2000, by H. Albrecht et al., from Germany [36]. At present days, the application of the GMAB process is mostly found in the automotive industry where galvanized AHSS is popularly used [28]. The fundamental technology of GMAB is the same as the conventional GMAW process but it uses lower melting temperature filler wires relative to the base metal, as shown by the schematic in Figure 2.3 (a) [28]. In the GMAB process, the primary purpose of arc plasma is to melt the filler wire which then transfers to the workpiece to create an

interfacial bond between workpieces and filler material [28]. This is shown clearly in Figure 2.3 (b) and (c) which show the difference in fillet weld made by GMAW and GMAB respectively. Copper-based filler materials are typically used for GMAB in the automotive industry (i.e., silicon-bronze (CuSi3Mn1) and aluminum-bronze (CuAl8)) which have a melting point in the range of 1000–1100°C.

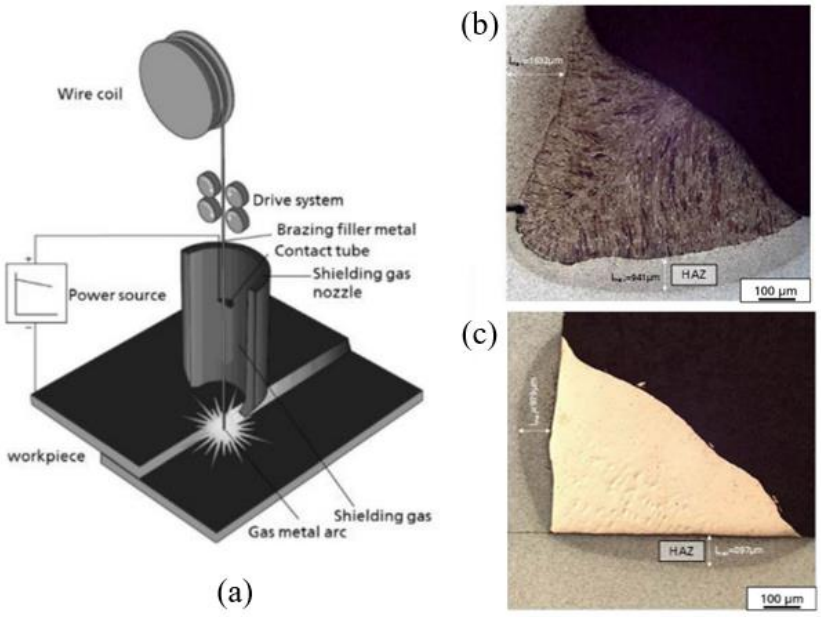

Figure 2.3: (a) Schematic of the GMAB process; (b) cross-section of regular fillet weld; (c) cross-section of the brazed seam. Obtained from Andreazza et al. [25]

2.3.1 Process variables

The process variables of the GMAB process are the same as the conventional GMAW process as both joining techniques share the same fundamental technology of the GMA process [28]. The process variables of the GMAB process are as follows:

1. Wire feed speed (WFS) – The user defines WFS to control the filler wire feeding rate. The GMA machine automatically adjusts the current to match the WFS such that the arc length is kept consistent. [28].
2. Voltage – The user defines voltage to control the arc length. The amount of voltage is proportional to the arc length [28].
3. Travel speed (TS) – Also referred to as welding speed, the user defines travel speed to control the rate of welding or brazing. The TS has a direct impact on the heat input and amount of filler material deposition per unit length of brazing [28].
4. Torch angle and position – The orientation at which the torch head is angled and positioned with respect to the workpiece [28].
5. Shielding gas – The choice of shielding gas plays a large role in the formation of arc and heat input. Pure argon or a mixture of argon and CO_2 is most commonly used for the GMAB process [28].
6. Metal transfer mode – Modern GMA machines often have several built-in programs that allow for various metal transfer modes. In the GMAB process, the metal transfer modes that allow low heat input with high controllability are used; for example, short circuit transfer mode, pulse mode, and cold metal transfer (CMT) mode are typically used for GMAB applications [13,37–39].
7. Material – In the GMAB process, base metal workpieces are joined by dissimilar materials (i.e., steel base metals using copper-based filler material). Therefore, the type of filler material and the base metal workpiece must be chosen appropriately for a successful GMAB process [28].

2.4 Fundamentals of GMAB

2.4.1 Effect of WFS, voltage, and TS

Among the process variables of the GMAB process, WFS, voltage, and TS are considered the most important control input as they directly control the heat input and filler material deposition which have a direct consequence on the bead geometry, microstructure, and mechanical properties of the joint [37–41]. As the WFS controls the rate of filler material deposition and amount of current, increasing WFS results in the increase of overall bead size, and has a flattening effect where the melt pool spreads more, increasing the bead width. When the arc length becomes longer by increasing the voltage, it also has a flattening effect similar to the increase of WFS due to the increase in momentum of the droplet transfer, but the overall bead size is unchanged [42]. It also tends to increase a spatter due to the unstable arc and high stirring force of the arc [24]. However, the voltage is kept low for the GMAB process to ensure short-circuit transfer of the droplets which allows for low heat input and high stability, which is critical for good quality braze bead. TS has a significant effect on bead quality as it directly determines the heat input and filler material deposition per unit length [24]. Increasing TS will drastically reduce heat input over the area which discourages the spreading of the molten pool, consequently decreasing the bead width and increasing the bead height. The effect of WFS, voltage, and TS on the bead quality is summarized in Table 2.1, and the cross-sectional image of the bead that shows the effect of WFS and TS is shown in Figure 2.4.

Table 2.1: General effect of the WFS, voltage, and TS on the brazing quality [28,43]**.**

INCREASE OF:	HEAT INPUT	BEAD WIDTH	BEAD HEIGHT	BEAD SIZE	SPATTER
WFS	↑	↑	↓	↑	↑
VOLTAGE	↑	↑	↓	Unchanged	↑
TS	↓	↓	↑	↓	↑

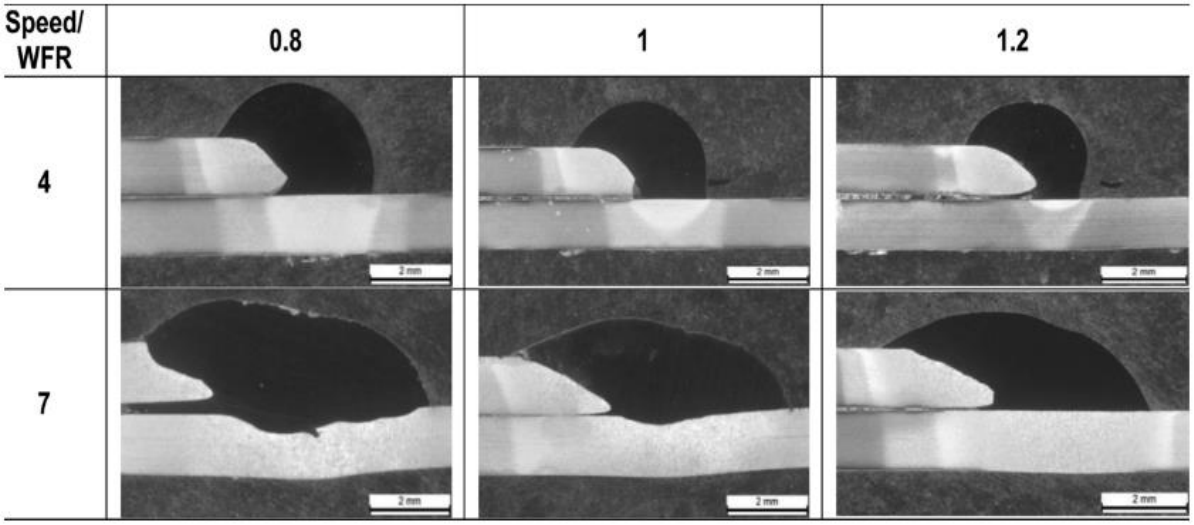

Figure 2.4: The cross-section of the beads illustrating the effect of WFS and TS. The units are in m/min. Obtained from Singh et al. [39]

The researchers often use calculated heat input as an input variable to study the responses instead of using individual control variables (WFS, voltage, TS). The heat input over unit length by the system is typically calculated by using eq 1 [44].

$$q = \frac{V * I}{TS} * \varepsilon \qquad \text{eq 1}$$

Where q is heat input, V is voltage, I is current, TS is travel speed, and ε is the efficiency of the GMAB process.

2.4.2 Intermetallic compound

An Intermetallic compound (IMC) is an alloy that contains two or more metallic constituents and has its own crystal structure, phase, orientation, and properties that are different from that of parent metals [45]. In the GMAB process, the formation of the IMC

phase plays important role in creating a joint in two ways; first, the IMC layer acts as an interlayer that binds the steel and copper matrix together; second, dispersed IMC phase formed acts as precipitates that strengthens the braze bead via dispersion strengthening mechanism [46,47]. Figure 2.5 shows the steel and Si-bronze (CuSi3Mn1) interface from the GMAB process, which clearly shows the base metal (steel), IMC layer, copper matrix, and precipitates. The type of IMC formed entirely depends on the type of workpiece and filler material used. However, the overall formation mechanism and the role it plays are similar.

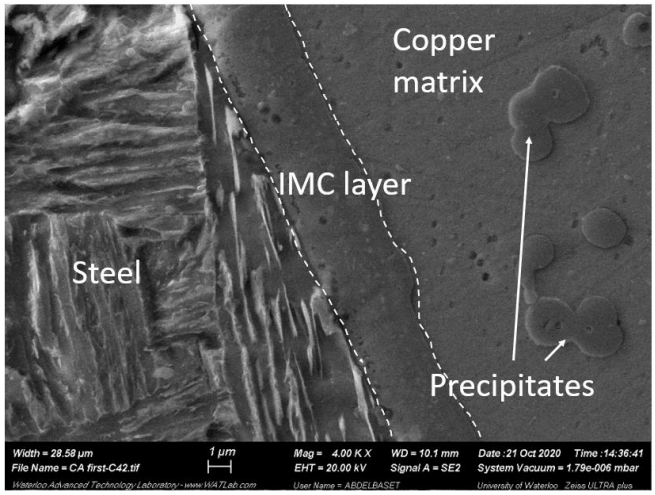

Figure 2.5: SEM image of IMC layer at steel-copper interface created by the GMAB process between DP600 steel and silicon bronze filler material.

The dispersed IMC phase and IMC layer formed during GMA brazing of the lap joint are shown in Figure 2.6 (b) and (c) respectively. During GMAB, the IMC layer is formed by the diffusion of Fe atoms directly from the steel substrate which subsequently reacts with Si atoms from the filler material [39,46,48]. Therefore, the thickness of IMC layer is a good indicator for the local heat input because it controls the peak temperature and cooling rate which governs the diffusion of Fe atoms that promotes the growth of the IMC layer [37,39].

Indicated as partial-melted-zone (PMZ) Figure 2.6 (a), partial melting of the top sheet provides a majority of Fe atoms necessary to form the IMC with Si atoms from the filler material, which is dispersed throughout the bead driven by the stirring effect of the arc pressure. The inhomogeneity in size, shape, and composition is often observed for the dispersed IMC phase, as shown in Figure 2.6 (b). This is likely to be attributed to the fact that nucleation, growth, and distribution of the IMC phase are largely affected by the inhomogeneous temperature profile in the bead due to the nature of the heat source (arc), as well as the stirring effect of the arc pressure [49]. Due to these effects, the precipitate density was also observed to be inconsistent in the bead such that a higher density of precipitate was generally observed in the outer region relative to the center region as indicated in Figure 2.6 (a) [50].

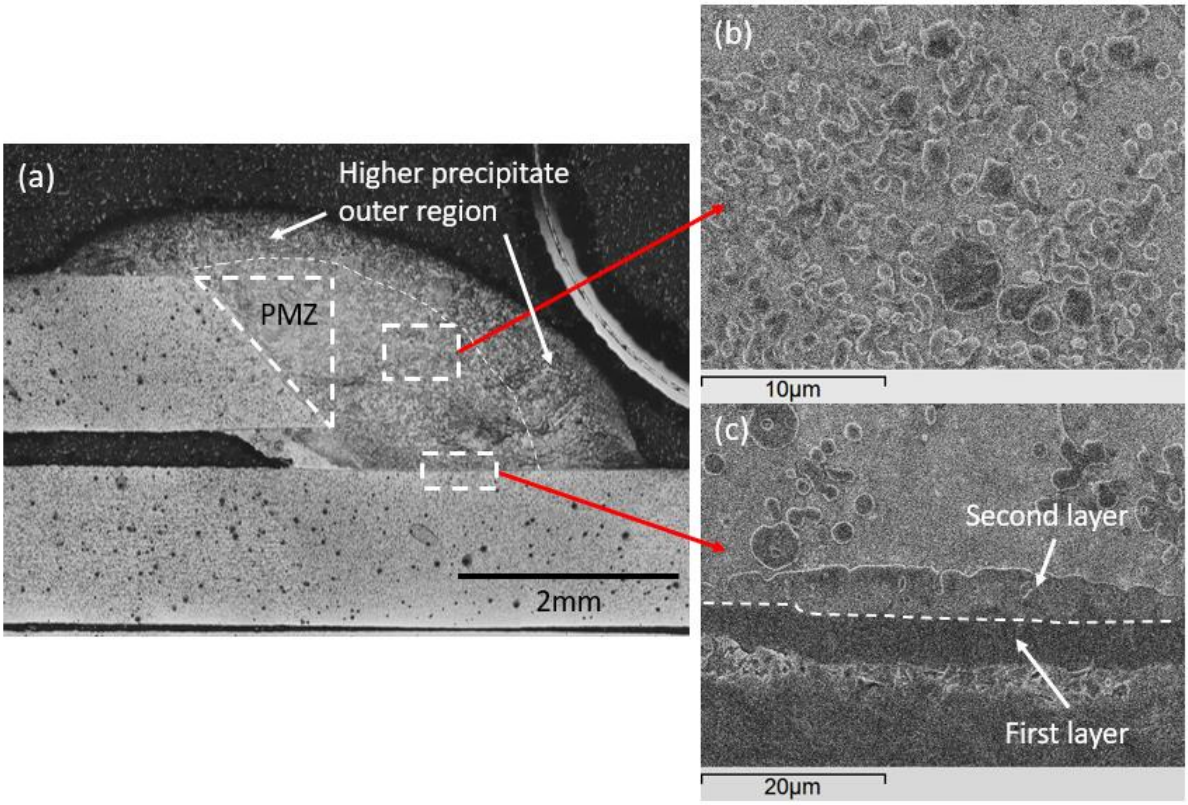

Figure 2.6: Different types of IMC formed in the GMA brazing of steel substrate in lap joint configuration using a CuSi3Mn1 filler wire:(a) cross-section of braze bead, (b) dispersed IMC phase at the fusion zone, (c) IMC layer at the interface.

2.4.3 Mechanical properties

Existing literature has shown that the GMA brazing with copper-based filler material can reach 100% joint efficiency using 800 MPa range base metals (i.e., DP800 and TRIP 800) [13,37–39,51,52]. This is mostly attributed to the dispersion strengthening effect of the dispersed IMC phase in the braze bead, which was shown to increase the strength of a braze bead close to the strength of base metal [37,39]. This means that the strength of braze bead also heavily depends on the heat input as it controls the amount of dispersion and formation of the IMC phase. Singh et al. [39], clearly showed in Figure 2.7 (a) that the amount of

dispersed IMC phase increase with the increase of heat input. Consequently, the joint strength is also directly proportional to the heat input, as shown in Figure 2.7 (b).

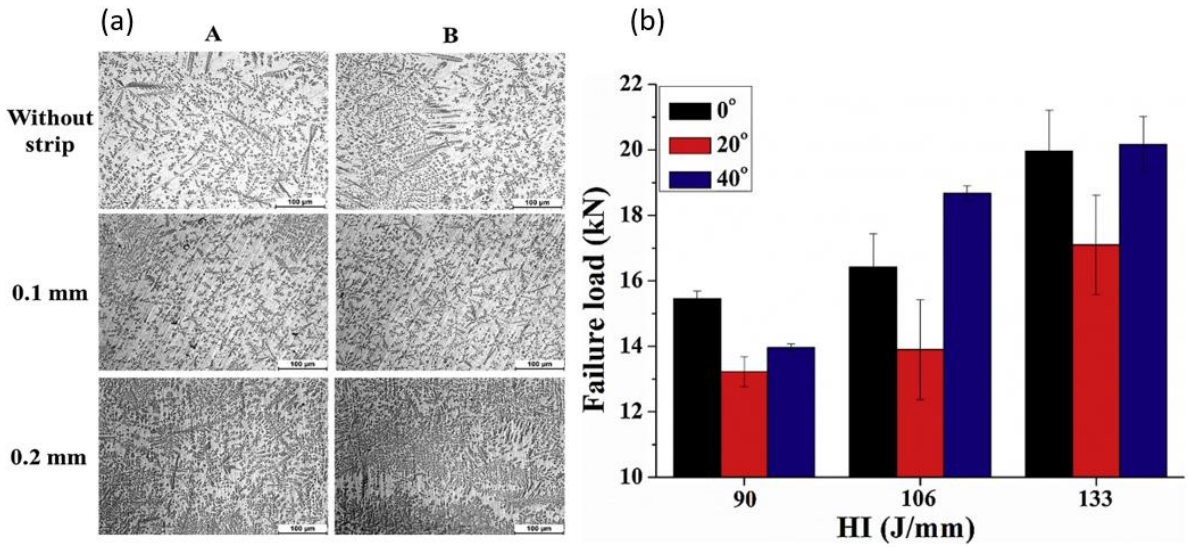

Figure 2.7: Effect of heat input on: (a) dispersed IMC phase, (b) joint strength for increasing heat input (noted as HI). Obtained from Singh et al. [39]

During lap-shear tensile testing of GMA brazed lap joint, five types of fracture modes were typically observed as shown in Figure 2.8: interfacial fracture (IF), vertical interface fracture (VI), braze bead fracture (BB), heat-affected-zone (HAZ), and base metal fracture (BM) [37,39]. Note that VI and BB failure modes, and HAZ and BM failure modes were sometimes considered the same in the literature [13,37]. According to S. Basak et al. [37], fracture mode shifted from IF → BB → HAZ/BM with the increase of joint strength when the heat input is increased. This phenomenon was explained as followings,

1. IF failure occurs at low heat input due to the improper development of interfacial bonding (IMC layer) due to insufficient time. As a result, a crack propagates along with the bottom interface at a low tensile load.

2. BB or VI failure occurs with the increased heat input and bead size due to the formation of properly developed interfacial bonding that avoids IF failure.
3. HAZ or BM fracture occurs when the heat input and bead size are further increased due to the sufficient strengthening of the braze bead and bead size that successfully prevents crack propagation into the braze bead.

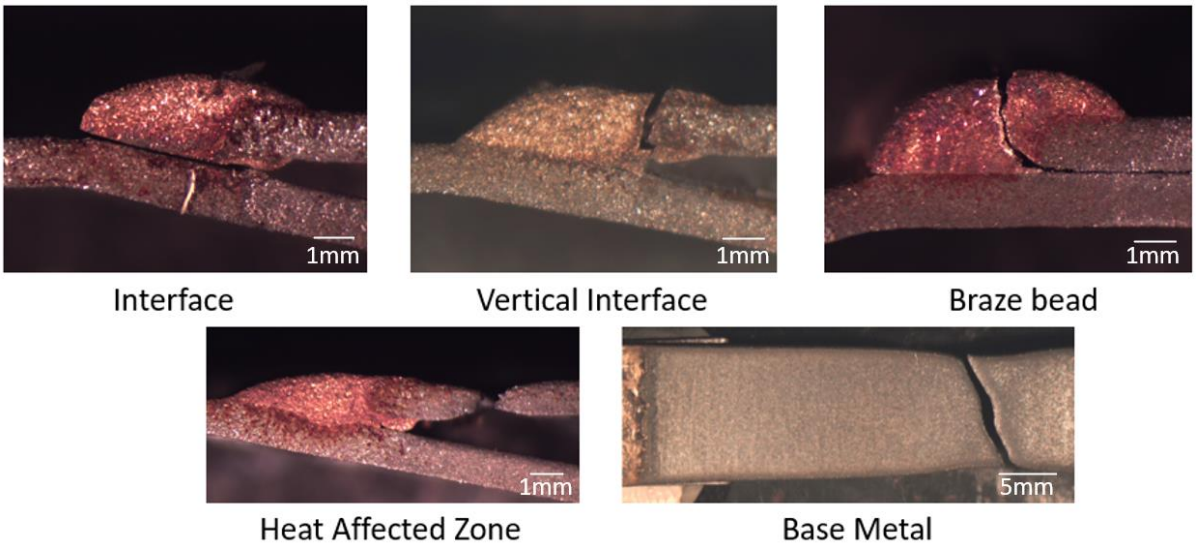

Figure 2.8: Five types of facture modes observed during lap-shear tensile testing of a GMA brazed lap joint.

2.5 Effect of torch position and angle

Torch angle and position refer to the GMAB torch head's location and its relative angular orientation with respect to the workpiece. Only a few researchers have investigated the effect of torch angle and position for the GMA brazing of steel sheets in lap joint configuration. Basak et al. [37] performed a GMAB experiment with push mode (i.e., below 90°) and pull mode (i.e., above 90°) of the torch travel angle (angle parallel to the travel direction). It showed that the push mode had superior joint performance compared to the pull

mode. Singh et al. [39] studied the effect of work angle (i.e., angle of torch perpendicular to the travel direction) on the joint quality which showed that superior wettability and joint strength were observed when the work angle is increased. However, both studies only showed the mechanical result of varying torch angles with a preliminary explanation for the cause of such phenomenon. Therefore, further research is needed to explain the role of torch position and angle in more detail.

2.6 Effect of gap clearance

GMAB is fundamentally different from the conventional brazing process. In soft soldering and brazing, a gap-brazing mechanism takes place where the workpiece is heated to the melting temperature of the filler material which allows the molten filler material to spread through the gap, driven by capillary action [28]. In GMAB, spreading and wetting of molten filler material does not rely on capillary action due to the extremely fast heating and cooling rate of the process. Instead, the spreading and wetting of molten filler material are driven by external forces such as arc pressure, surface energy, and gas flow [28,53]. Perhaps this is the reason why there is no existing literature that studies the effect of gap clearance during the GMAB process for lap joint configuration.

However, according to Goland and Reissner [54], the eccentricity of the tensile loading in a single lap joint induces a bending moment at the overlapping region. This results in the development of a stress concentration composed of peel stress and shear stress at the root region as shown in Figure 2.9 [55,56]. During tensile testing, cracks were always initiated at the root region and propagated into the bead for all the samples that had showed BB failure mode [37,39,57]. The presence of gap clearance would greatly change the geometry of this region under stress concentration, which may have a great impact on the mechanical properties of the GMA brazed lap joint.

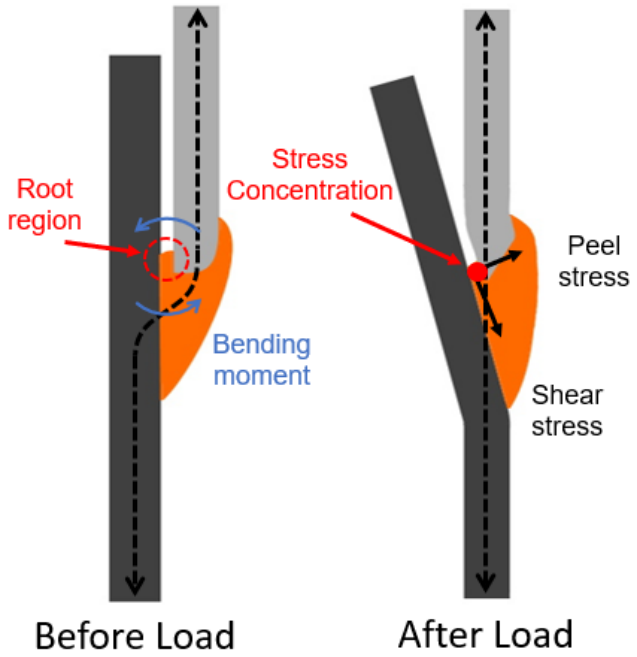

Figure 2.9: The stress development in a braze joint due to the eccentricity of the load that creates a stress concentration at the root region.

2.7 Effect of zinc coating

The effect of zinc coating type (GI and GA) during the GMAB process was studied by Khan et al. [50], who performed a GMAB experiment on a bead-on-plate configuration to show the effect of coating type on the wettability of molten Si-bronze filler material and microstructure of the bead. The most apparent difference between each coating type was shown at the tail-end region of the wetting, where a much higher Zn concentration was observed for a GI-coated sample and showed distinctive microstructure in this region. This microstructurally and chemically different region at the tail-end area is known as zinc-rich-area (ZRA), which is also found elsewhere in literature that studies arc or laser brazing applications on Zn-coated steels [58–61]. However, further research is needed to investigate the effect of Zn-coating type on the mechanical properties of a joint.

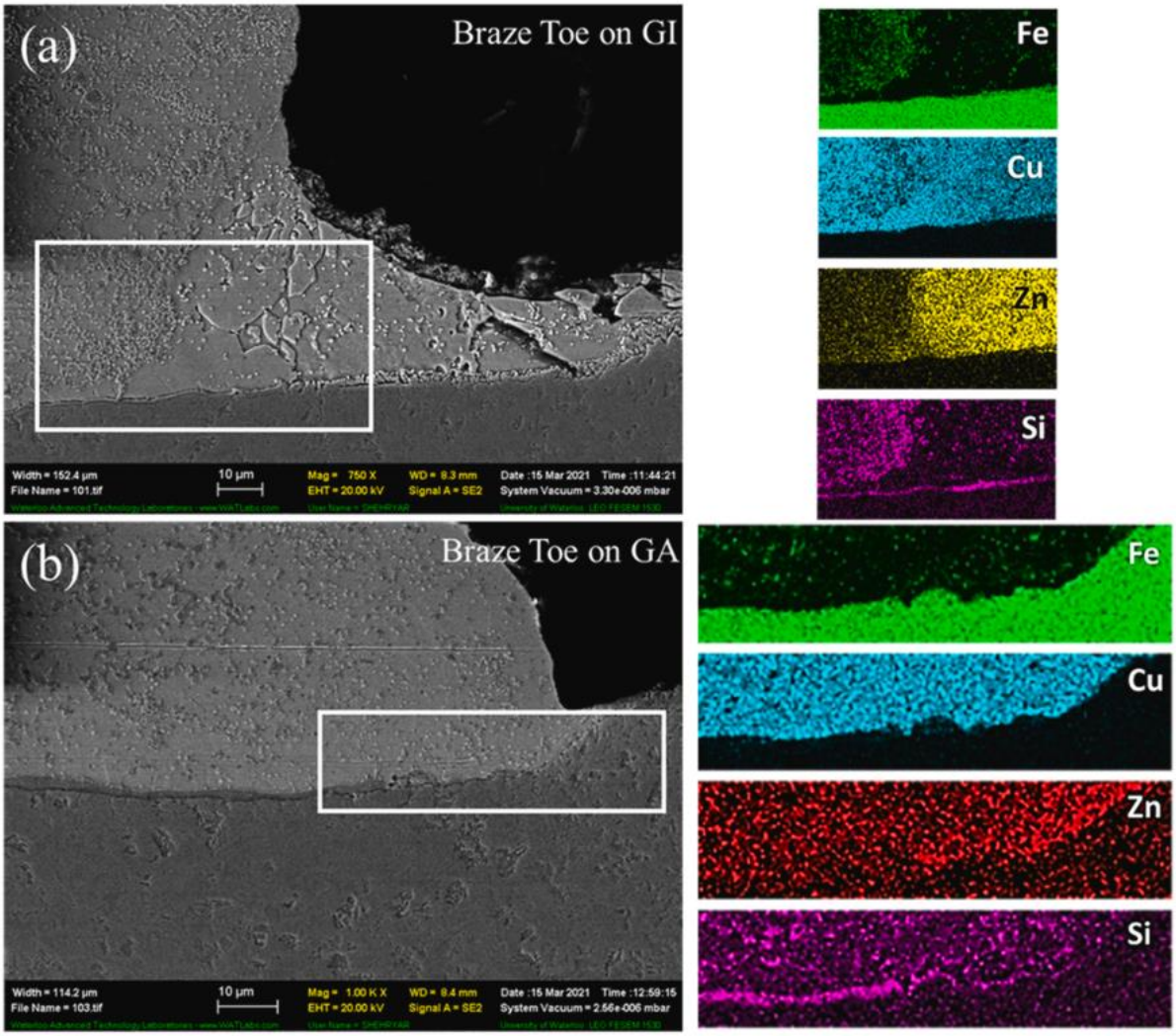

Figure 2.10: Effect of Zn-coating type on the microstructure and chemical composition at the tail-end region of the bead-on-plate arc brazed sample. Obtained from Khan et al. [50]

Chapter 3

Methodology

3.1 Material details

1.4 mm thickness DP600 steel sheets with two different coating types (GI and GA) are used as a base metal workpiece. All base metals were cut to the dimension of 100 mm x 200 mm such that the rolling direction is perpendicular to the longer edge. Only GA DP600 is used for the study discussed in Chapter 4 and Chapter 5, and both GI and GA coated DP600 are used for the study in Chapter 6. 0.9 mm diameter CuSi3Mn1 (AWS ERCuSi-A) filler wire was used for all experiments in this thesis. The detailed chemistry and associated properties of the base metal and the filler wire are shown in Table 3.1and Table 3.2 respectively.

Table 3.1: GI and GA-coated DP600 base metal chemistry and coating properties.

	Base metal chemical Composition (Mass %)							Coating Weight (g/m^2)		Coating Chemistry (Mass%, Bal Zn)	
	C	Mn	Si	Cu	Al	Fe	Cr, Ti, B, Nb, Ni, Sn, Mo, V, P, S, N	Top	Bottom	% Al	%Fe
GI DP600	0.094	1.930	0.160	0.130	0.030	Bal	0.143	51	51.6	0.25	0.49
GA DP600	0.091	1.986	0.150	0.032	0.025	Bal	0.113	51.3	50.1	0.2	8.3

Table 3.2: Chemical composition and mechanical properties of the Silicon-bronze filler wire.

Filler material Composition (Mass%, Bal Cu)				Properties			
	Si	Mn	Fe	Diameter	UTS	Elongation	Hardness
CuSi3Mn1	2.9	0.8	0.02	0.9mm	374 MPa	58.80%	89.6 HB

3.2 GMAB experiment

3.2.1 Equipment detail

A Lincoln Electric PowerWave® R500 (DCEP) power supply controlled by a FANUC Robot ARC Mate 120© welding robot was used to perform GMAB experiments in lap joint configuration with the setup shown in Figure 3.1 (a). The welding program chosen for the experiments was the precision pulse mode for Silicon Bronze (SiBr) filler wire. Figure 3.1 (b) shows the GMA brazed sample where the braze seam is made along the longer edge (200 mm) of the base metal workpiece with an overlap distance of 10 mm. The schematic of the fixture and setup is shown in Figure 3.1 (c) which describes the method for gap clearance control by using thin metal shims and clamping of the base metals on the fixture. The process parameters which were kept constant for all experiments are summarized in Table 3.3. For the experiment performed for Chapters 5 and 6, work and push torch angles of 25° and 10° are used respectively.

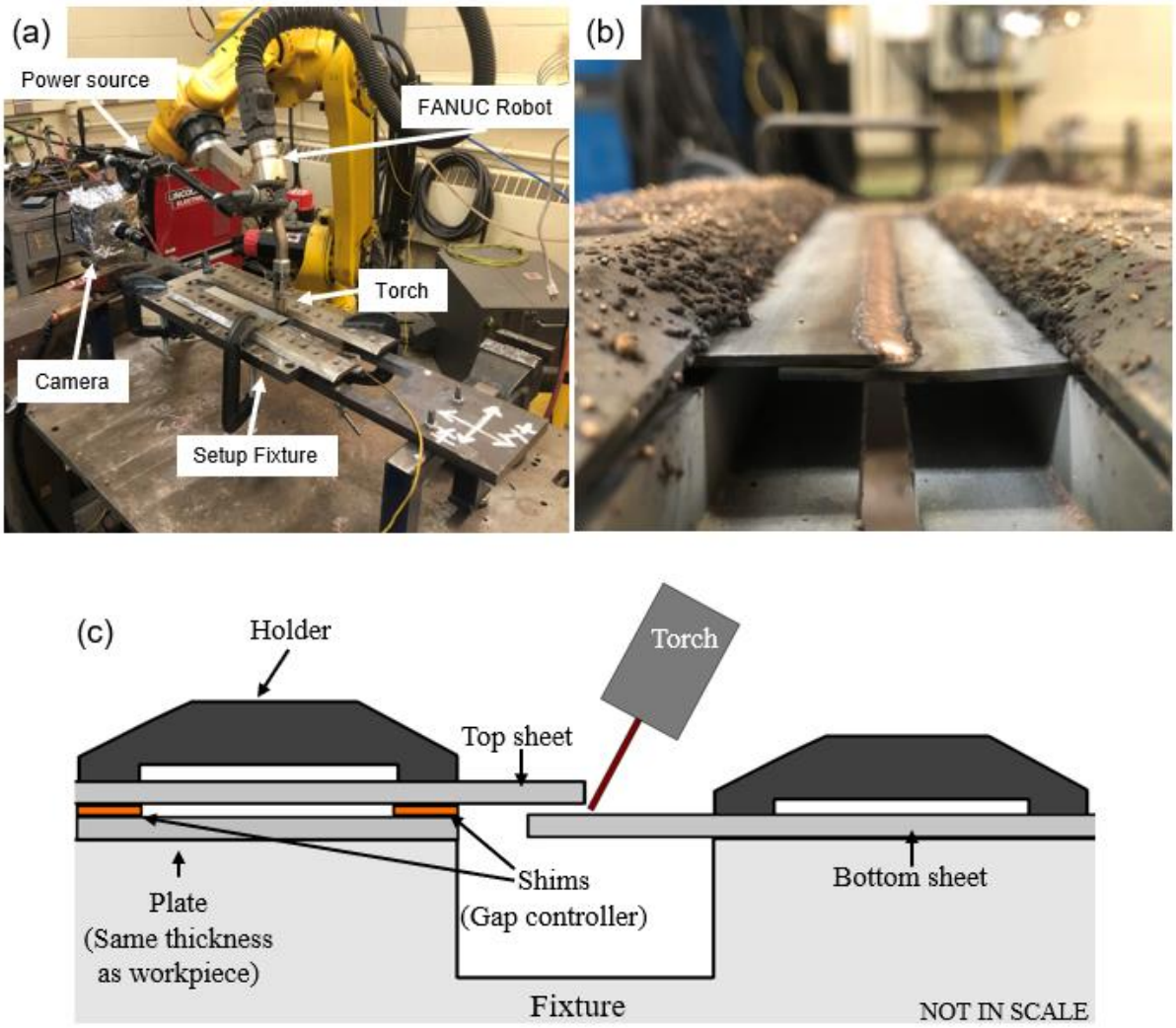

Figure 3.1: GMA brazing experiment setup: (a) setup environment, (b) GMA brazed sample (c) schematic of setup. Obtained from Cho et al. [73]

Table 3.3: MIG brazing process parameter.

Welding Mode	Power Supply	WFS (m/min)	TS (m/min)	TRIM (Voltage)	CTWD (mm)	Gas Type	Gas Flow Rate (cfh)
Precision Pulse	PowerWave ® R500 (DCEP)	7.6	1	0.5	15	100 %Ar	14.2

3.2.2 Plasma cleaning surface treatment

In Chapter 5, plasma cleaning surface treatment is used as the method to control the wetting behavior of the molten filler material through the gap clearance. All base metals were degreased with ethanol prior to the GMAB experiment. For the base metals which required plasma cleaning surface treatment, Tergeo Plasma Cleaner manufactured by PIE Scientific LLC (Figure 3.2) is used for 15 min to plasma thoroughly clean the base metal surface.

Figure 3.2: Tergeo Plasma Cleaner manufactured by PIE Scientific LLC used for plasma cleaning surface treatment.

3.3 Sample preparation

The optical microscopy (OM) samples were mounted in conductive resin, then ground and polished using an automatic polisher in 5 stages as shown in Table 3.4. The polished samples were etched using ferric chloride etchant for 3–4 seconds.

Table 3.4: Grinding and Polishing steps used for optical microscopy sample preparation

	Stage 1	Stage 2	Stage 3	Stage 4	Stage 5
Disc	MD-Piano 80	MD-Allegro	MD-DAC	MD-NAP	MD-NAP
Suspension	Water	Diapro Allegro 9um	3µm diamond	1µm diamond	0.25µm diamond
Speed (RPM)	250	250	250	250	250
Force (Bar)	8	8	8	4	2
Time (min)	1	2	3	3	2

3.4 Imaging and recording data

3.4.1 High-speed imaging

In Chapter 4, the highspeed camera is used to capture the droplet transfer and molten pool during the GMA brazing experiment. Photron Fastcam Mini UX100 highspeed camera equipped with the RICOH F2.8/50 mm lenses (FL-CC5028-2M) and 700-1650 nm bandpass interference filter was used to record the GMAB process at 3200 fps.

3.4.2 Power input data

The power input data was acquired through an external multimeter connected with a separate National Instruments data acquisition module (USB-6000) that measured the current and voltage data in real-time using the LabVIEW software.

3.4.3 Optical Microscopy

Optical microscopy (OM) images are obtained by Clemex CMT (v. 8.0.197) manufactured by Les Technologies Clemex Inc which has mosaic imaging capability in

addition to the microhardness test capability. For higher magnification images, Zeiss Leo 1530 field-emission scanning electron microscopy (FE-SEM) is used.

3.4.4 Chemical analysis

For chemical analysis, energy dispersive X-ray spectroscopy (EDX) analysis was done using Zeiss Leo 1530 FESEM. JEOL JX-8230 electron probe micro-analyzer (EPMA) is used to create the elemental map discussed in Chapter 6.

3.4.5 Digital image correlation

MTS tensile frame with a load cell capacity of 100 kN equipped with a 3D Digital Image Correlation (DIC) system was used to conduct the lap-shear tensile testing to analyze the displacement and map of the strain in the brazing area. Stereoscopic DIC software, Vic 3D R9.1, from Correlated Solutions Inc was used for the analysis.

3.5 Mechanical testing

3.5.1 Tensile testing

A water-jet cutter was used to cut 50 mm gauge length tensile coupons from GMA brazed sample plates with the dimension specified in the ASTM E8/E8M-16a standard [62]. Instron Tensile Tester Model 4206 was used to perform lap-shear tensile test at a crosshead speed of 2 mm/min until fracture under quasi-static loading conditions.

3.5.2 Hardness measurement

The microhardness testing was performed using Clemex CMT (v. 8.0.197) manufactured by Les Technologies Clemex Inc with a dwell time of 10s. The indentation load of 200 gf and 5 gf are used for the studies discussed in Chapter 4 and Chapter 6 respectively.

Chapter 4

Effect of torch angle and position

In this chapter, the effect of torch angle and position on the location of droplet transfer, the behavior of arc, resulting bead geometry, and the mechanical properties of lap joints have been investigated in detail for the GMA brazing of GA DP600 using CuSi3Mn1 (i.e., Si-Bronze) filler wire in lap joint configuration.

4.1 Design of experiment and definition

The torch angle and position are defined as work angle (α), push angle (β), and torch position (*TP*), as shown schematically in Figure 4.1. The relevant details of each experimental run performed are shown in Table 4.1. The level of each parameter was chosen experimentally based on a pre-defined acceptable braze bead quality within the physical limitations of the torch position using the welding set-up shown in Figure 3.1.

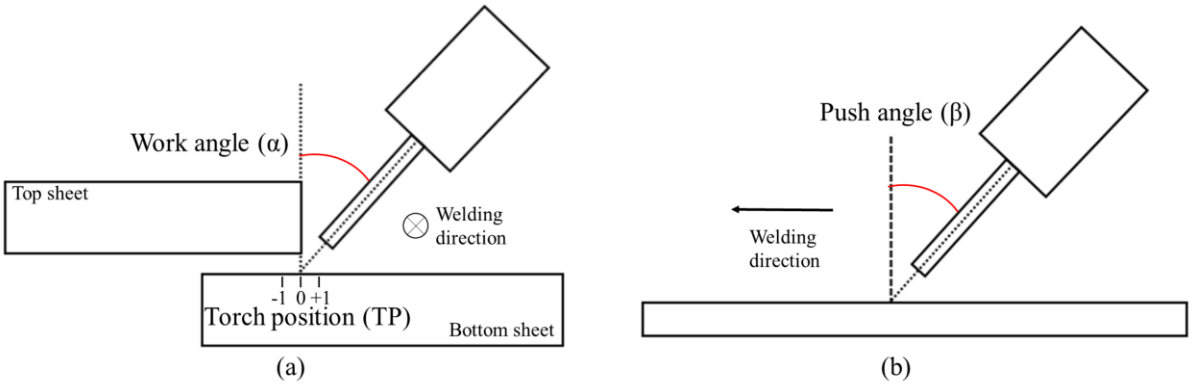

Figure 4.1: Definition of torch angle and position: (a) torch position (TP) and work angle (α) (welding direction is into the page); (b) push angle (β).

Table 4.1: Design of experiment (DOE) used and power input details.

Control Variables				Power Input	
Sample#	TP	Work (α°)	Push (β°)	I_{avg}	V_{avg}
1	1	10	0	95.3	18.9
2	-1	10	0	115.8	16.1
3	1	10	30	107.8	16.2
4	-1	10	30	108.5	17.1
5	1	40	0	99.6	18.0
6	-1	40	0	101.1	16.9
7	1	40	30	110.2	15.8
8	-1	40	30	115.4	17.4
9	1	25	10	103.3	17.3
10	-1	25	10	101.1	18.2
11	0	10	0	115.7	17.4
12	0	10	10	115.5	16.2
13	0	10	20	117.6	15.8
14	0	10	30	109.9	16.4
15	0	25	0	106.8	18.4
16	0	25	10	118.6	16.4
17	0	25	20	115.6	16.1
18	0	25	30	109.5	16.7
19	0	40	0	104.3	17.4
20	0	40	10	103.7	16.7
21	0	40	20	104.9	17.0
22	0	40	30	105.1	17.5

To analyze the bead geometry, the cross-section of the braze bead was measured according to the schematic shown in Figure 4.2, where W is the width of the bead, L_1 is the leg length measured from the edge of the top sheet to the toe of the braze, L_2 is the wetting length of the braze interface along with the bottom sheet, H is the bead height, S is the throat length, θ is the toe angle, PMZ_1 refers to the partially melted zone at the top sheet, and PMZ_2 refers to the partially melted zone at the bottom sheet. The measurements of the bead

geometry were taken from 3 brazed samples for each experimental condition and expressed as an average as shown in Appendix A.

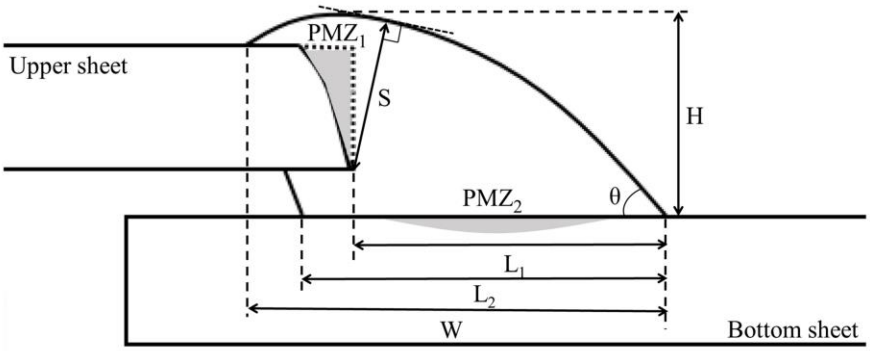

Figure 4.2 Schematic showing the bead geometry measurement.

4.2 Effect of torch position and angles on arc behavior and bead geometry

To investigate the effect of torch position and angles on the arc behavior, the melt pool formation, and the resulting bead geometry, the GMAB process was observed using a high-speed camera, and the images were captured at the different points of the precision pulse mode waveform, i.e., background current, ramp start, and droplet contact during the pulsing sequence, as shown in Figure 4.3. It is important to note that the typical precision pulse mode only has a single peak. However, during the GMAB process, the second peak is formed due to the sudden drop in resistance during short-circuiting at the moment of droplet contact. Figure 4.4 shows the images captured from a high-speed camera and the final cross-section of the bead. Note that the images at the background current and ramp start position are saturated by the arc plasma due to its sheer light intensity, but it has been shown by Dos Santos et al. [63] that this ‘arc-light-saturation’ sufficiently represents the actual arc behavior.

The effect of torch position and angles on bead geometry was represented statistically using the main effect plots shown in Figure 4.5. The L_1/W ratio (Figure 4.5 a) represents the overall position of the bead with respect to the edge of the top sheet, and the H/W ratio (Figure 4.5 b) represents the width of the bead relative to the height.

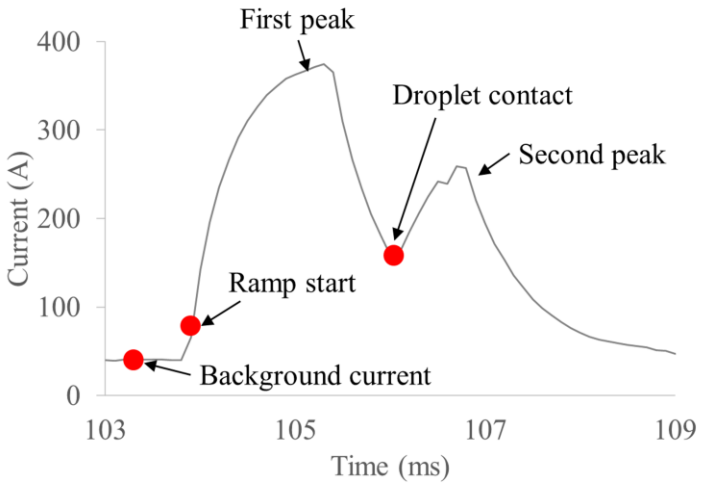

Figure 4.3: Typical pulse waveform observed during the GMAB experiment. As indicated by the red dots, a high-speed camera is used to capture the moment of background current, ramp start, and droplet contact. Note that typical precision pulse mode only has the first peak. The second peak is formed during brazing application due to the sudden drop in resistance when the short circuit is formed at the moment of droplet contact.

The effect of torch position, TP, was analyzed by comparing samples 9 and 10, shown in Figure 4.4 (a) and (b), respectively. The TP was changed from +1 mm to -1 mm while α and β were kept constant at a value of 25° and 10°, respectively. The change in arc shape was observed at the background current and ramp start where the position of the arc relative to the workpiece shifted from the bottom sheet to the upper corner of the top sheet as the TP increased from +1 mm to -1 mm. This type of change in the arc shape and location is due to

the change in distance between the electrode tip and the workpiece. Based on Ohm's law, the amount of current flow is inversely proportional to the resistance, which in this case was provided by the gap between the electrode tip and the workpiece. Consequently, during the DCEP process, electrons flow out of the workpiece towards the electrode following the path where the arc length is the shortest. It was also observed in Figure 4.4 (b) that there was a clear deflection of the molten droplet towards the top sheet at a TP of -1 mm at the moment of droplet contact. This can be attributed to the electromotive force (EMF), defined as the Lorentz force which is induced by the cross product of the current flow and the magnetic field, causing this force to act inwards towards the direction of the current flow [64,65]. As the shortest arc length is formed close to the top sheet, the current flows towards the arc through the top sheet, and consequently, the Lorentz force pushes the droplet towards the flow of current. Figure 4.5 (a) shows that TP has a dominant effect on the L/W ratio. This is due to the direct consequence of the shift in the location of the arc position and the change in the location of the molten droplet deposition due to the change in TP. Figure 4.5 (b) clearly shows that TP also has the most significant effect on the H/W ratio. When TP was -1 mm, a major portion of the molten filler material was deposited closer to the top sheet increasing the H/W ratio. As the TP was increased to +1 mm, more filler material was deposited onto the bottom sheet making the bead flatter and wider resulting in a lower H/W ratio. This direct influence of TP on the location of the arc and the location of droplet transfer has a significant effect on the size of PMZ_1 as shown in Figure 4.5 (d).

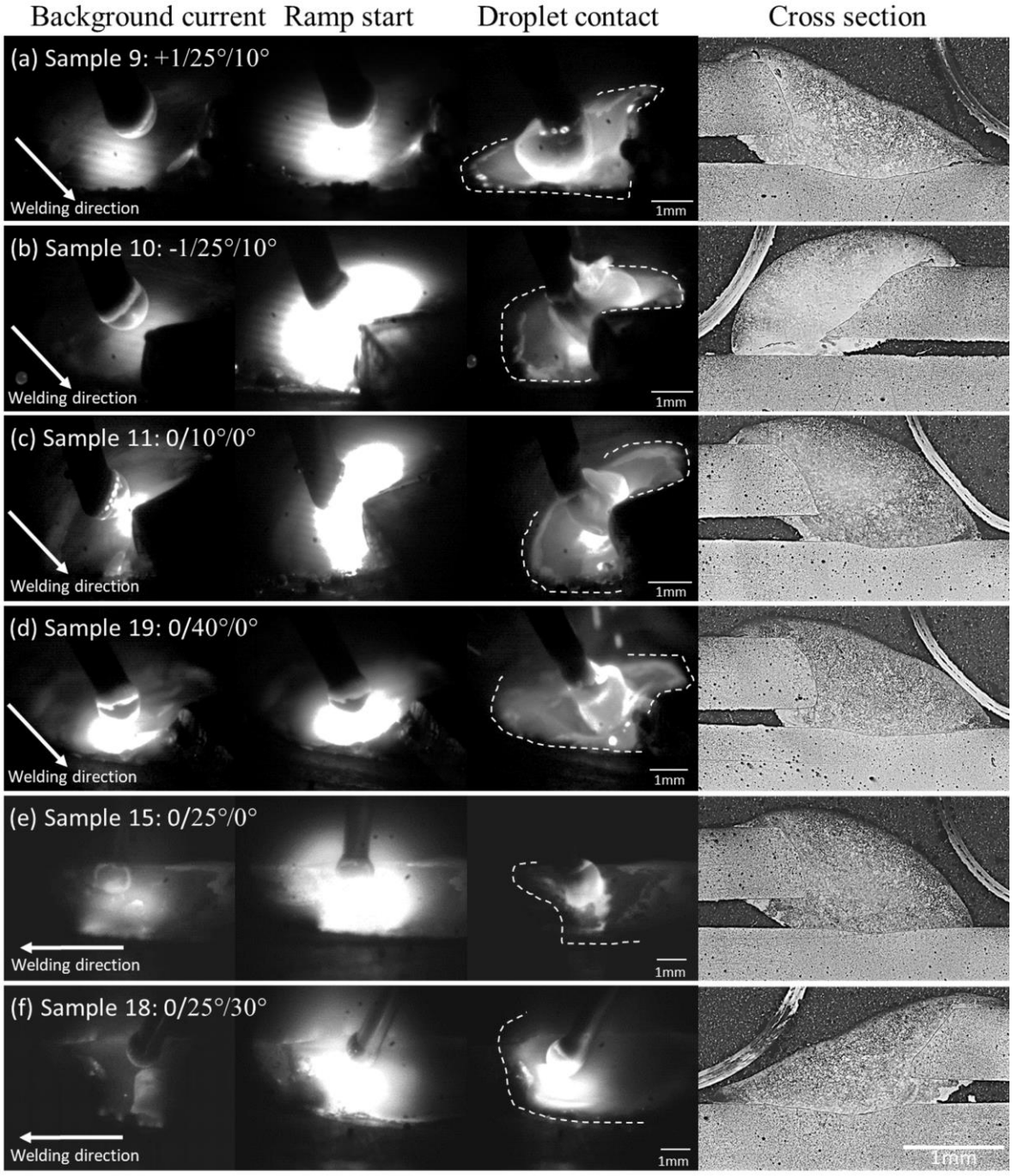

Figure 4.4: High speed images of arc brazing process at the moment of background current, ramp start, droplet contact, and the resulting cross-section of the bead: (a) sample 9 (TP= 1mm, α=25°, β=10°), (b) sample 10 (TP= -1mm, α=25°, β=10°), (c)

sample 11 (TP=0mm, α=10°, β=0°), (d) sample19 (TP=0mm, α=10°, β=40°), (e) sample 15 (TP=0mm, α=25°, β=0°), (f) sample 18 (TP=0mm, α=25°, β=30°). [Note that the scale of all micrographs is the same as the one shown in the final Figure]

The effect of work angle, α, was illustrated by comparing samples 11 and 19 (in Table 4.1), shown in Figure 4.4 (c) and (d), respectively. The value for α was changed from 10° to 40° while TP and β were kept constant at 0 mm and 0°, respectively. Interestingly, the effect of α was shown to have a very similar effect to TP but to a lesser extent. Such an effect can be attributed to the way in which the wire is fed to the workpiece. When α was set to 10°, as shown in Figure 4.4 (c), the filler wire was closer to the top sheet which caused the arc to have greater interaction with the top sheet. The deflection of the molten droplet towards the top sheet was also observed when α was set to 10°, similar to that was observed when TP was set to -1 mm. Consequently, this resulted in a lower L_1/W ratio when α was set to 10° compared to when it was set to 40° (Figure 4.5 a), in which case the filler wire was fed closer to the bottom sheet, which resulted in the arc having greater interaction with the bottom sheet. However, it was clearly seen in Figure 4.4 (d) that the droplet transfer also occurred at an angle along with the wire, which was deposited at the root of the bead, similar to when TP was set to 0 mm. This difference in the location of the arc position and the molten droplet deposition diminished the severity of the change in the bead geometry which resulted in the diminished effect of α on bead geometry, as shown by the main effect plot in Figure 4.5, which shows that effect of α follows the same trend as TP but to a lesser extent.

The effect of the push angle, β, was illustrated by comparing samples 15 and 18 which corresponds to Figure 4.4 (e) and (f), respectively. The value of β was changed from 0° to 30° while TP and α were kept constant at 0 mm and 25°, respectively. The most significant effect of β was on the melt pool behavior at the moment of droplet contact. As β was increased, the melt pool was pushed towards the front of the wire. This inherently increased the time that the melt pool was exposed to the arc and slowed down the cooling rate of the melt pool, allowing it to spread more easily on the substrate, subsequently forming a wider

bead width. This observation was confirmed by the main effects plot shown in Figure 4.5 (c), which showed that β had the most significant effect on bead width W. As W increases, it can be seen that H decreases naturally to maintain the geometric and volumetric constraints of the braze joint. This results in a decrease in the H/W ratio, as shown in Figure 4.5 (d). Additionally, it was observed that the effect of β on W further increases with an increase in angle, especially above 20° as shown by the main effect plot in Figure 4.5 (c).

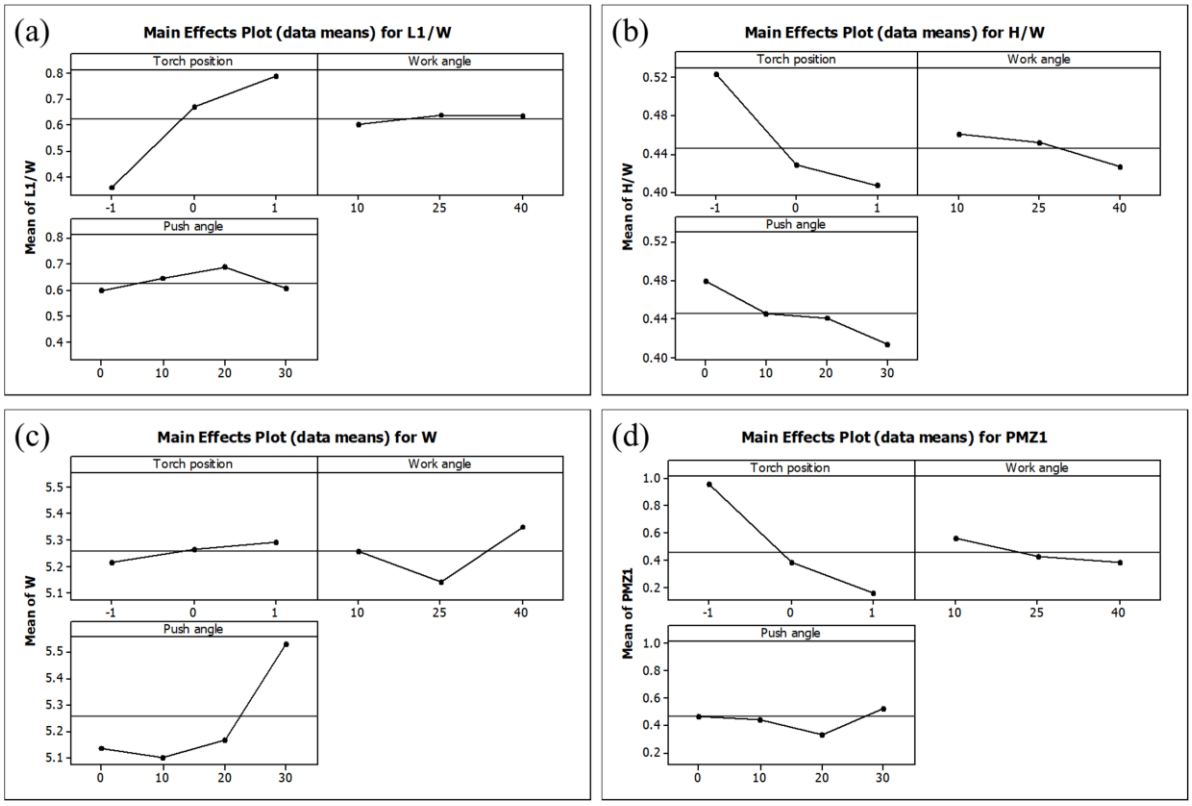

Figure 4.5: Main effect plots of torch position and angles for bead geometry: (a) L_1/W ratio, (b) H/W ratio, (c) W, (d) PMZ_1

4.3 Effect of torch position and angles on heat input

The previous section confirmed that the location of the arc and the droplet transfer behavior are sensitive to the torch angle and postion. This is directly related to the heat input distribution across the workpiece since the main source of heat transfer in the GMA process is the arc plasma and the droplet transfer [66]. The effect of angle and position on the heat input across the workpiece was investigated by analyzing the HAZ formed at the base metal, as shown in Figure 4.6. The hardness profile across the HAZ at the top and bottom base metal was taken as the physical representation of the heat input, similar to what has been reported in the literature [67], as shown in Figure 4.7.

4.3.1 HAZ formation

Two distinct regions within the HAZ were identified in the brazed samples, as shown in Figure 4.6 (a). The coarse-grained HAZ (CGHAZ) was shown to be composed mainly of lath martensite with a small portion of bainite and ferrite. The fine-grained HAZ (FGHAZ) had a dual-phase microstructure, composed mostly of martensite and ferrite. Figure 4.6 (b) shows the predicted CCT diagram for the base metal chemistry shown in Table 3.1. Based on the microstructure of the CGHAZ shown in Figure 4.6 (a) and the CCT diagram shown in Figure 4.6 (b), the cooling rate at the CGHAZ can be estimated to be close to 100 °C/s with the peak temperature being higher than the Ac_3 temperature of 819°C. Although actual peak temperature is difficult to determine, it can be deduced that the temperature at the CGHAZ was high enough for the original dual-phase microstructure to fully transform into austenite (γ) and the γ-grains in the fully austenitic matrix. During cooling at a rate close to 100 °C/s the fully austenitic microstructure of the CGHAZ is transformed into coarse grains of martensite with sparsely dispersed islands of bainite and ferrite. At the peak temperature below Ac_3 (819°C) but above Ac_1 (676.1°C), partial austenitization occurs and the microstructure is composed of very fine γ and α-ferrite grains [37,68]. Then, during cooling, the fine γ grains transform into highly refined martensite and bainite and form the microstructure of the FGHAZ [37]. The relative increase in the phase volume fraction of the

martensite in the bulk microstructure is directly responsible for the increase in the hardness of CGHAZ and FGHAZ [69]. The hardness of the base metal was measured to be about 220 HV, while the average hardness of the FGHAZ was about 250 HV. The CGHAZ had the highest average hardness which was measured to be greater than 290 HV. The region where the hardness values transitioned from about 270 HV to 290 HV was designated as the transition zone between the FGHAZ and CGHAZ. Therefore, the peak temperature at the HAZ region with a hardness value of 230 HV (FGHAZ start) and 290 HV (CGHAZ start) can be roughly estimated as 676.1°C (Ac_1-austenite start) and 819°C (Ac_3-austenite complete), respectively.

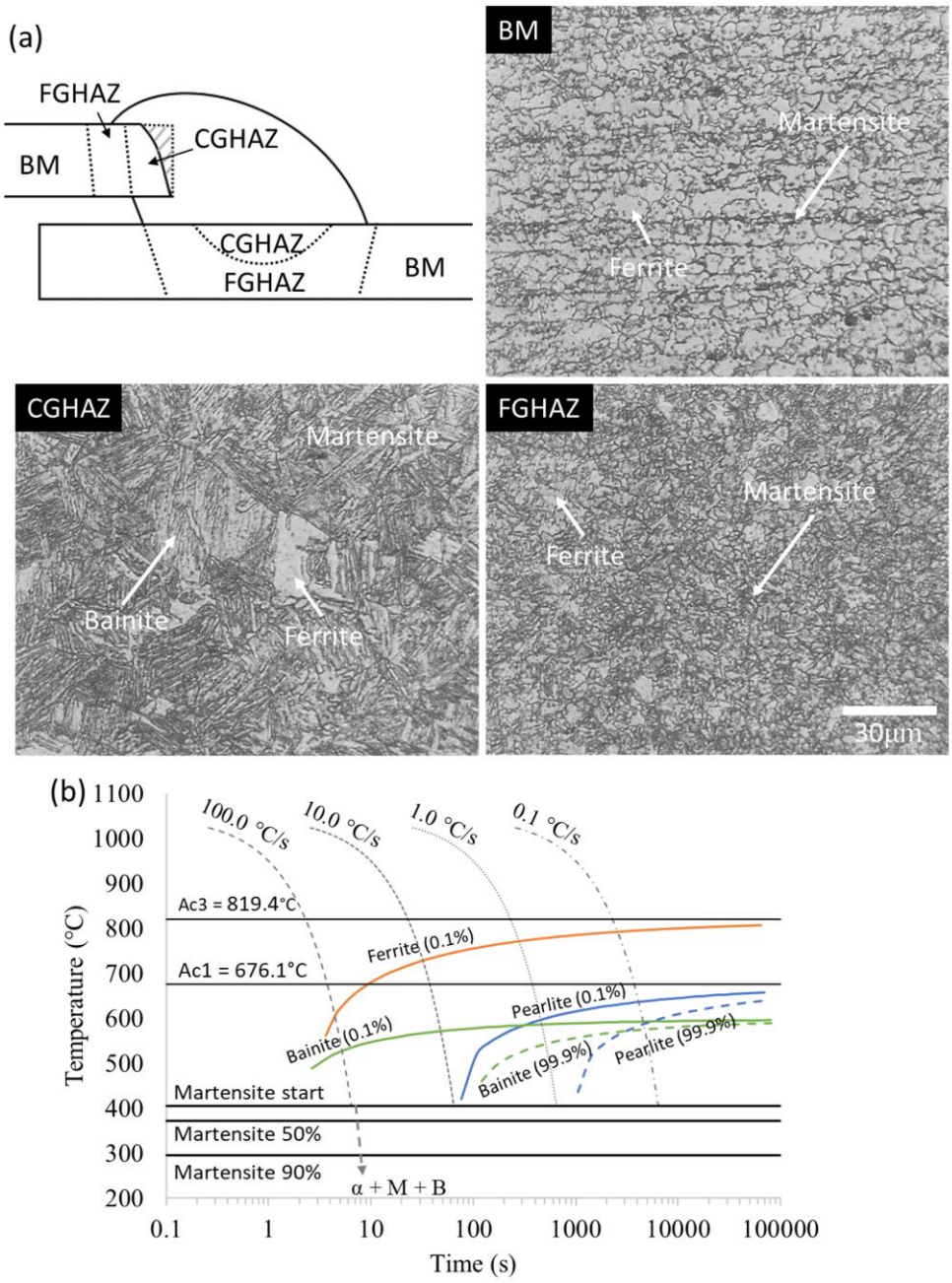

Figure 4.6: (a) OM images showing the microstructure of BM, CGHAZ, and FGHAZ regions developed during GMAB. All OM images are in the same scale. (b) CCT diagram generated for DP600 with given base metal chemistry generated by JMatPro. Based on the microstructural component, the CGHAZ region experienced a cooling rate close to 100 °C. (α: ferrite, M: martensite, B: bainite)

4.3.2 Heat distribution

The hardness profiles across the HAZ for all the samples are shown in Figure 4.7. The size of the HAZ was measured based on the location of the HAZ boundary which was determined by the increase in the hardness value beyond the base metal hardness, as shown in Figure 4.7 (b). It is important to note that the difference in the maximum hardness observed in Figure 4.7 (b-e) was the direct consequence of different peak temperatures that the workpiece experiences due to the change in the torch parameter. The higher the peak temperature, the longer the workpiece temperature exceeds the Ac_1 temperature, which increases the phase volume fraction of the austenite in the matrix and the subsequent austenite grain size, which then transforms into martensite during cooling, which changes the hardness properties of the HAZ.

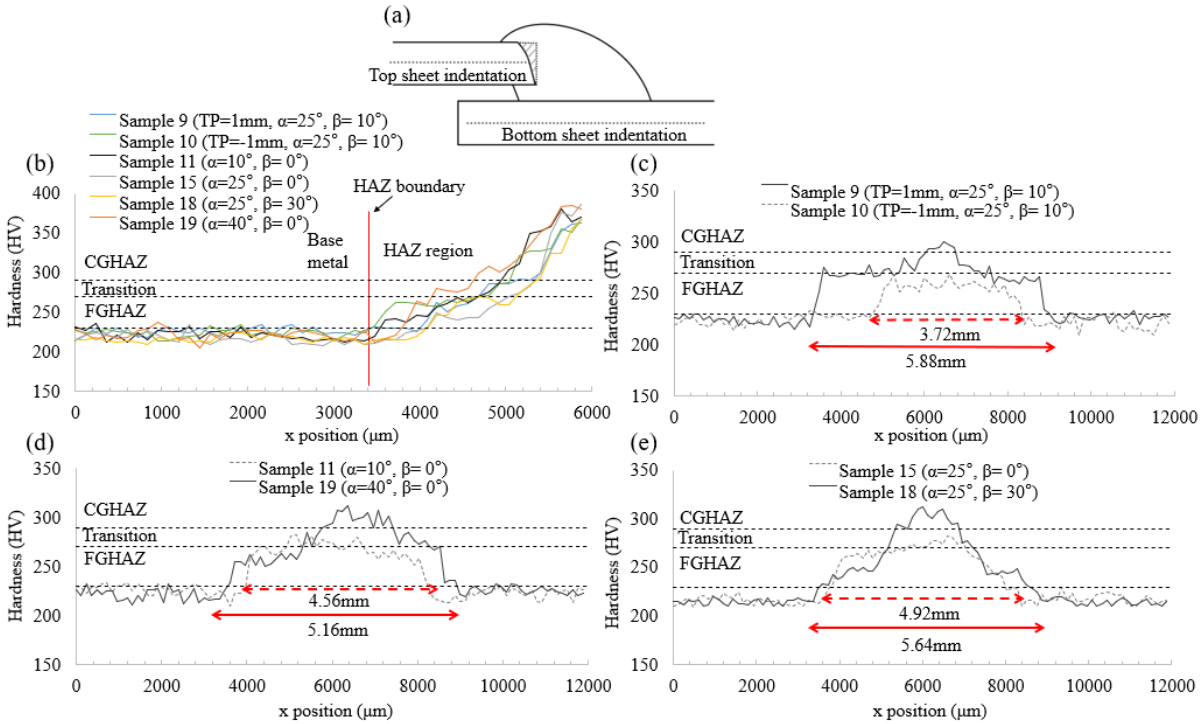

Figure 4.7: The effect of parameters shown by the hardness profile at the base metals: (a) schematic showing how the indents were made; (b) hardness at top sheet for all samples discussed in Figure 4.4; (c) hardness profile at bottom sheet for sample 9 and

10 (effect of TP); (d) hardness profile at bottom sheet for sample 11 and 19 (effect of α); (e) hardness profile at bottom sheet for sample 15 and 18 (effect of β). The indents were spaced 120 μm apart and total of 50 and 100 indents were made on the top and bottom sheets, respectively. The range of hardness for each HAZ region is indicated by the dotted line. The size of HAZ is measured and shown by the red both sided arrows

Figure 4.7 (b) shows the hardness profile of the top sheet for samples 9, 10, 11, 15, 18, and 19. All the samples showed an increase in hardness to about 350 HV close to the edge of the top sheet. The difference in a gradient of hardness profile can be observed for each sample but the large variation in hardness values resulting from the inhomogeneous microstructure makes it difficult to visualize the effect with greater certainty. The HAZ boundary location appears to be similar for most of the samples because the datum along the x-position is at the edge of the top sheet near the braze interface which is dependent on the size of PMZ_1. Due to these limitations for the analysis of the top sheet, the hardness profiles across the bottom sheet, as shown in Figure 4.7 (c)-(e), were used to analyze the effect of torch position and angles on heat input.

The hardness profiles across the bottom sheet for samples 9 and 10 are shown in Figure 4.7 (c) to demonstrate the effect of TP on the heat input distribution. The size of the HAZ for samples 9 and 10 varied greatly, being measured at 5.88 mm and 3.72 mm, respectively, with a difference of 2.16 mm. This difference in HAZ size was the largest compared to that for the effect of α (0.6 mm) and β (0.72 mm), as shown in Figure 4.7 (d) and (e), respectively. This agrees with our previous observations, clearly showing that TP had the most significant influence on the bead geometry. In fact, the difference in L_2 (being measured at 2.51 mm, 0.67 mm, and 0.76 mm) was very similar to the difference in HAZ size (being measured at 2.16 mm, 0.6 mm, and 0.72 mm), for the samples representing the effect of TP (sample 9 and 10), α (sample 11 and 19), and β (sample 15 and 18), respectively. This shows that the HAZ size is directly related to the bead geometry – specifically to the wetting length.

The higher HAZ hardness of sample 9 (Figure 4.7 c) confirms that a higher peak temperature was experienced for sample 9 compared to sample 10. This makes sense because the location of the arc and the transfer mode shifted towards the bottom sheet with an increase in the value of TP. The hardness profile for samples 11 and 19 (Figure 4.7 d: effect of α) showed a significant hardness difference in the HAZ such that a higher peak temperature was experienced for sample 19, but the difference in the size of the HAZ was small (~0.67 mm). This confirms a very important finding that α can be used to effectively control the heat input without changing the bead geometry significantly. Furthermore, the shift of the CGHAZ towards increasing x-position was observed for sample 19 which must be due to the effect of the shift in the arc shape and its location, as shown in Figure 4.4 (c) and (d).

The hardness profile across samples 15 and 18 (Figure 4.7 e: effect of β) showed a significant difference in the peak hardness value of the HAZ, with a size difference of about 0.76 mm. Interestingly, sample 18 showed a noticeably larger FGHAZ region with an average hardness value of about 240 HV, which was not seen in the other samples. The slower cooling rate due to an associated increase in the value of β must be responsible for the development of a larger FGHAZ region. The significantly higher hardness value for sample 18 clearly shows that increasing the value for β increases the heat input into the workpiece.

4.4 Lap-shear tensile test

4.4.1 Fracture modes

To understand the effect of torch position and angles on the mechanical properties of the lap joint, GMA brazed samples were investigated using quasi-static shear tensile testing. Four types of distinct failure modes: IF, BB, HAZ, and BM failure modes were observed, as shown in Figure 4.8. There was a clear correlation between the elongation of the tensile samples and the failure mode, such that the lowest to greatest elongation was observed when the failure mode went from IF→BB→HAZ→BM. Similar joint strength was observed for

the samples that underwent BM and HAZ failure with the key difference being a slightly lower total elongation for the samples failing in the HAZ. Samples showing BB failure had a large range of elongation and strength as shown by the insets (BB-Low and BB-high) in Figure 4.8, with the sample failing at the root of the joint and the crack propagating through the braze. The samples showing IF failure always showed the lowest value of strength at failure and the lowest elongation. The detailed results of the shear tensile test performed in this study are presented in Appendix B.

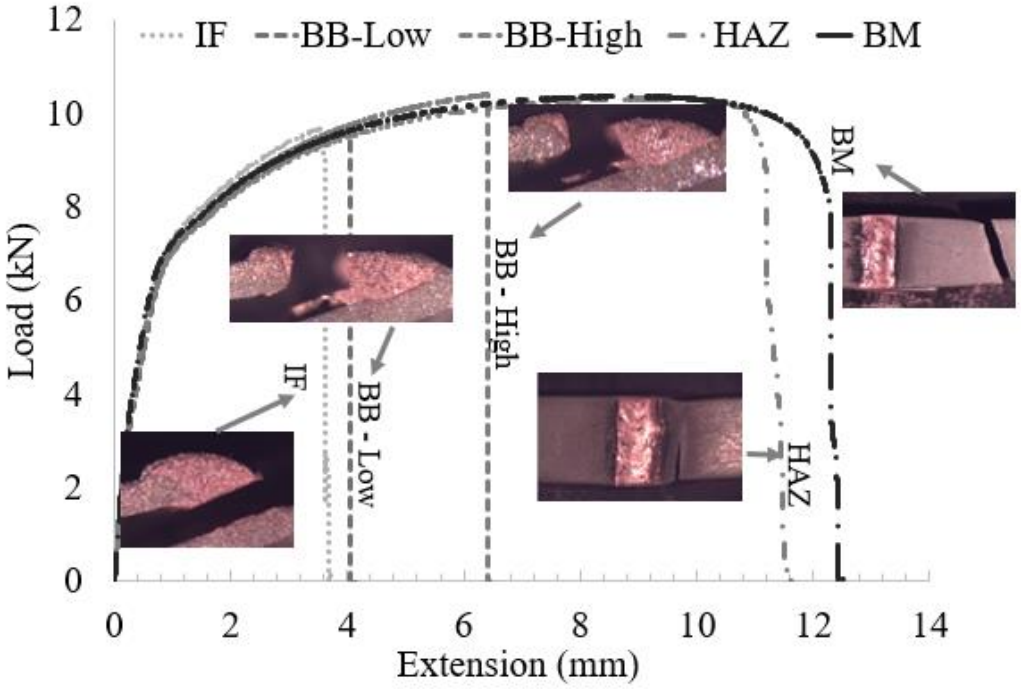

Figure 4.8: Load vs extension curve and stereoscopic images showing the four different failure modes: IF, BB, HAZ, and BM. A clear difference in extension is observed for each failure mode except BB failure which has a large range of strength and extension at failure.

4.4.2 Relationship between bead geometry and mechanical property

To investigate the relationship between bead geometry and joint strength, the scatter plots shown in Figure 4.9 were used to represent the tensile test results of all the shear tensile tested samples in terms of the geometric factors: L_1, PMZ_1, and S. It is worthy to note that the cluster of IF failed samples indicated in Figure 4.9 were the result of the improper formation of the bead geometry such that too much wetting happened at the top sheet as a direct consequence of the -1 mm of TP, which resulted in significantly poorer joint strength. Figure 4.9 (a) clearly showed that an insufficient L_1 was mainly responsible for the occurrence of the IF failure mode which happened mostly when L_1 was shorter than 3 mm. However, no other trend could be drawn from Figure 4.9 (a) because the samples showing BB failure had a wide range of strength which overlapped with the same region showing the cluster of samples that had BM and HAZ failure. A similar presence of samples showing BB failure was observed among the cluster of BM and HAZ failed samples relative to the value of throat size, S, as shown in Figure 4.9 (b). This was an unexpected result because the throat size (shown as S in Figure 4.2) is typically considered a very important factor in controlling the strength of lap joints made using conventional fusion welding techniques [28]. However, the throat size showed no apparent effect on the strength of braze bead for the samples that showed BB failure. Finally, a similar cluster of samples showing BM, HAZ, and BB failure was also observed relative to the size of PMZ_1, as shown in Figure 4.9 (c). This was also an unexpected result because the size of PMZ_1 indicates the amount of Fe diluted into the melt pool which affects the volume fraction of Fe-Si precipitates observed in the braze microstructure which have been reported to strengthen the braze bead by way of dispersion strengthening [40,70]. The results showed that too much dilution of Fe into the melt pool, which would lead to a higher volume fraction of Fe-Si precipitates, negatively affected the strength of the joints. To investigate this unusual behavior further, the microstructure of the braze bead was analyzed, as shown in the following section.

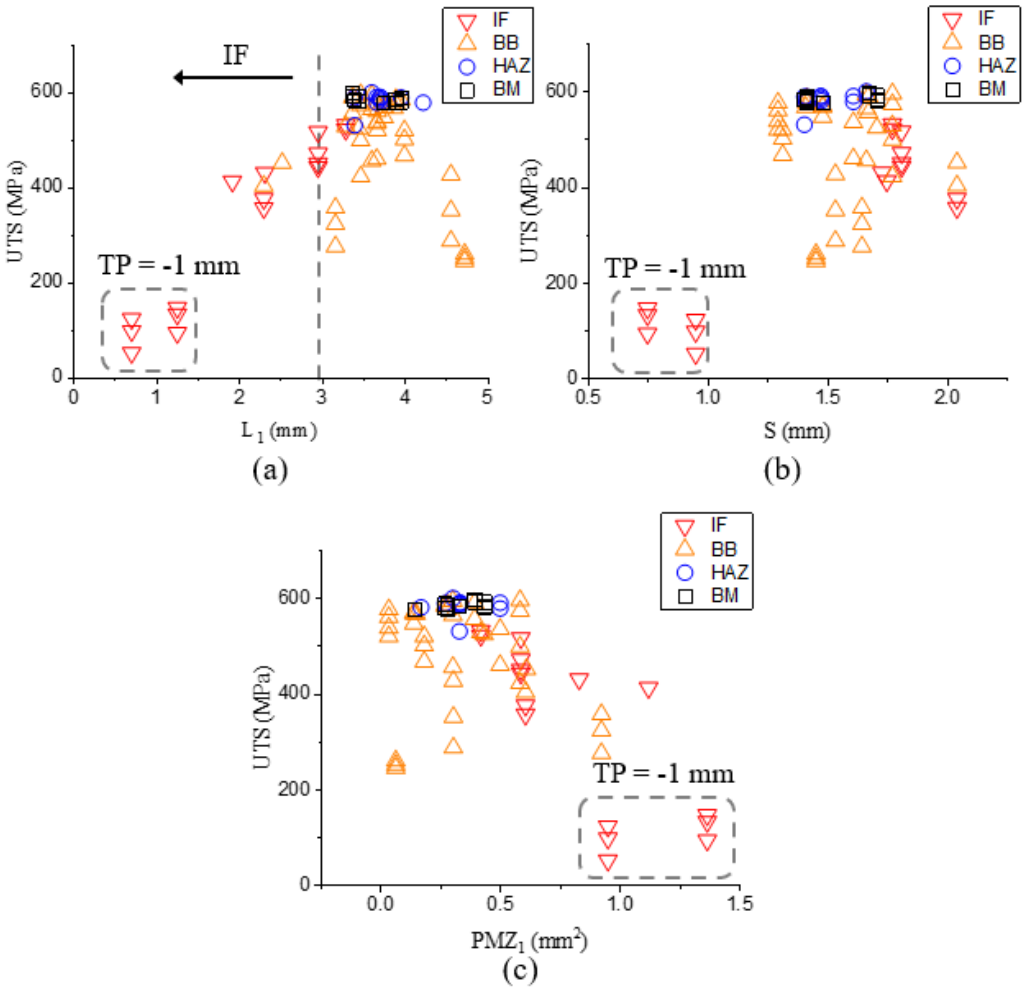

Figure 4.9: UTS and fracture mode obtained from shear tensile test plotted in terms of: (a) L_1, dotted line indicates that IF failure is most likely to occur when the value of L_1 is lower than 3mm; (b) S; (c) PMZ_1. The cluster of low strength IF failed samples indicated by the dotted box is due to TP of -1 mm.

4.4.3 Microstructure and morphology of braze bead

To explain the significant differences in the BB failure phenomenon associated with the strength and elongation of the tested samples, the microstructure of the braze bead for samples 15 (Figure 4.10 a, b) and 18 (Figure 4.10 c, d) were analyzed. A clear difference in

the morphology and the distribution of the precipitates within the Cu-matrix was observed between the samples. Numerous large Fe-rich secondary phase islands were observed in sample 15, which had a complex composition ranging between 72.79–85.56 wt.% Fe and 9.14–21.83 wt.% Cu with varying amounts of Si and Mn depending on the regions within the islands, as shown by the EDX results in Figure 4.11 (a). The clear martensitic morphology and chemical composition of these islands (Figure 4.11 a) suggest that these large Fe-rich secondary phase islands are undissolved Fe particles that entered into the melt pool directly from the steel substrate. On the other hand, sample 18 showed the presence of numerous, significantly smaller, homogeneously dispersed, and widely reported [39,71] Fe-Cu-Si precipitation-strengthening particles which formed during cooling when the solubility limit of Fe in solid-solution Cu was exceeded and the precipitation of these secondary phases was required to maintain the thermodynamic stability of the system. The chemical composition of the particles was found to be around 40.24–50.41 wt.% Fe and 43.38–57.44 wt.% Cu with the remainder being composed of Si, which was about half of the Fe content observed in the undissolved Fe-rich dispersion strengthening islands seen in sample 15. The literature on the subject [40,46,47,70] claims that these precipitates are Fe_5Si_3(Cu) intermetallic compound (IMC) phase, which would require the precipitates to have nearly 37.8 at% Si, which is not remotely close to what was measured in this study. However, it is possible that the process parameters used in this study provided a relatively lower HI that did not give enough time for the appropriate reaction between Fe and Si particles to form the Fe_5Si_3(Cu) IMC phase. In any case, the results indicate that the secondary phases forming within the solidified braze are significantly more complex in terms of morphology and chemistry compared to what has been reported in the literature and require further characterization, which goes beyond the scope of the current study.

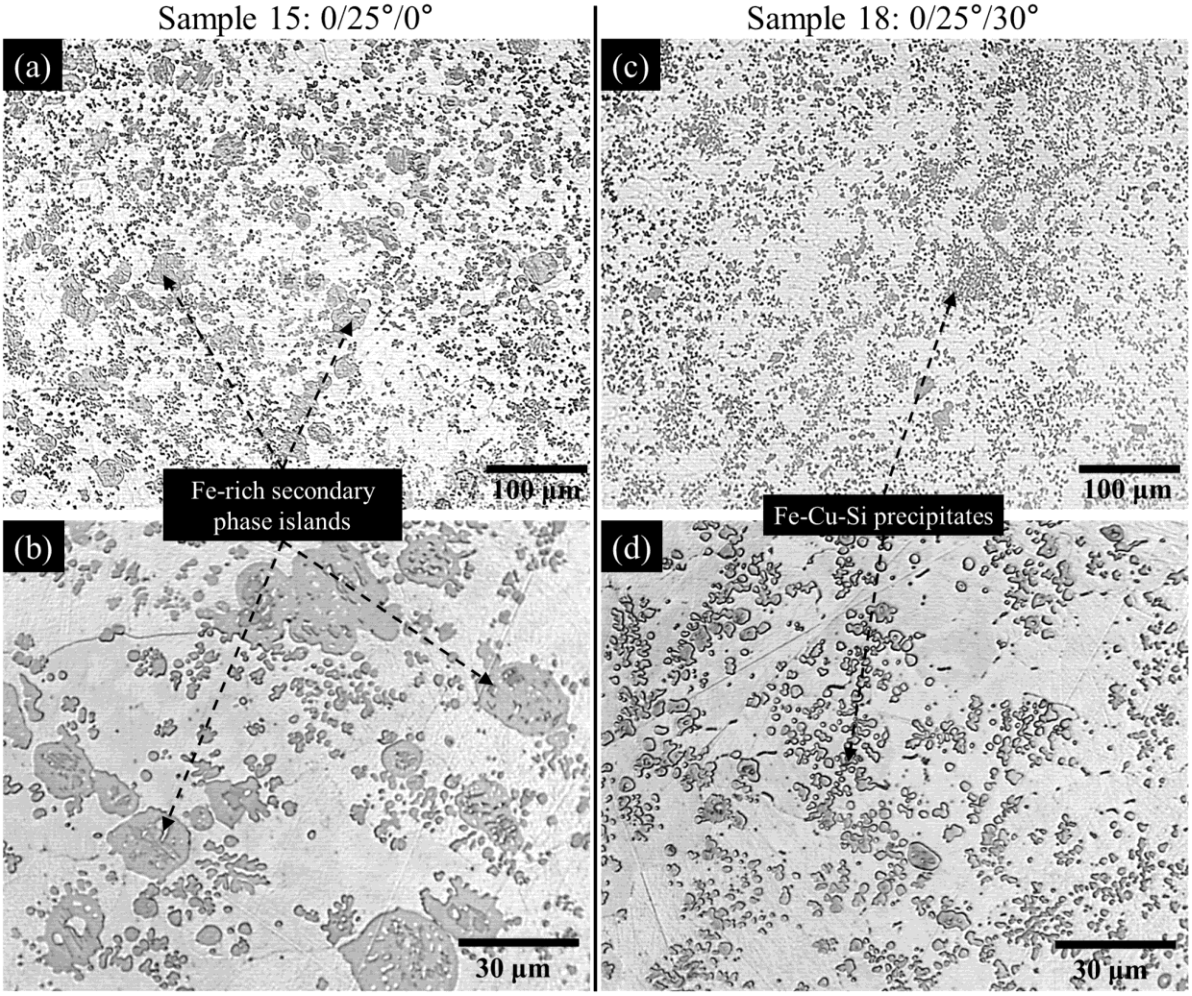

Figure 4.10: OM images showing Microstructure of braze bead showing a clear difference in morphology of precipitates: (a) sample15 at x100 magnification, (b) sample 15 at x400 magnification, (c) sample 18 at x100 magnification, (d) sample 18 at x400 magnification.

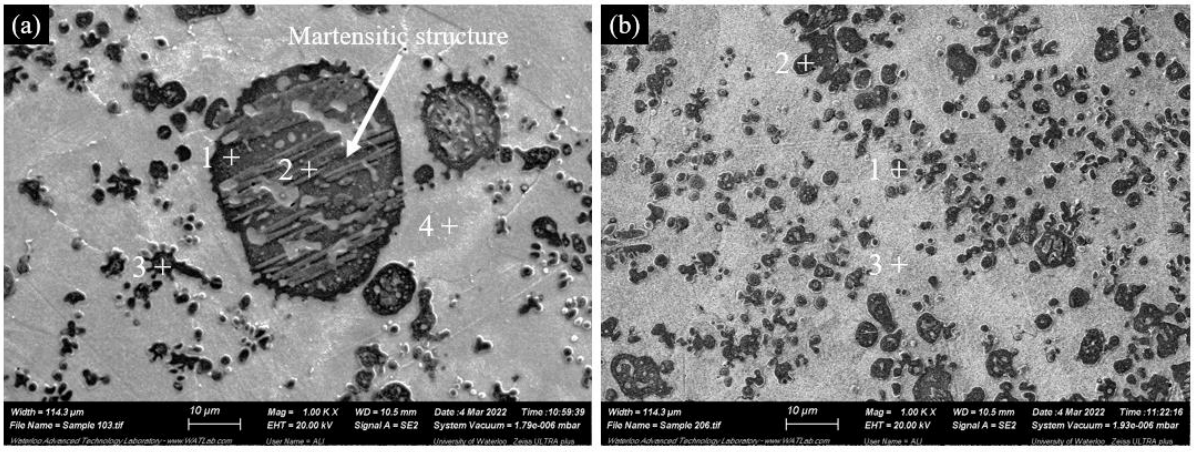

Region	SI wt% (at%)	Mn wt% (at%)	Fe wt% (at%)	Cu wt% (at%)
1	4.6 (9.0)	0.8 (0.8)	72.8 (71.4)	21.8 (18.8)
2	5.3 (10.1)	-	85.6 (82.2)	9.1 (7.7)
3	8.0 (15.0)	1.3 (1.2)	76.9 (72.4)	13.8 (11.4)
4	1.8 (3.9)	0.7 (0.8)	2.9 (3.2)	94.6 (92.0)

Region	SI wt% (at%)	Mn wt% (at%)	Fe wt% (at%)	Cu wt% (at%)
1	4.9 (9.8)	1.3 (1.3)	50.4 (50.6)	43.4 (38.3)
2	2.3 (4.8)	-	40.2 (42.2)	57.4 (53.0)
3	1.8 (4.0)	0.6 (0.7)	3.3 (3.6)	94.4 (91.8)

Figure 4.11: SEM image and EDX analysis result for braze bead of sample 15 (a) and sample18 (b) showing the clear difference in chemical composition and morphology of Fe-Cu-Si precipitate between two samples.

The clear difference in the morphology and chemical composition of the secondary islands and precipitates observed in Figure 4.10 was due to the change in β from 0° to 30°. By setting a low value of β, the cooling rate of the melt pool was increased, which most likely resulted in the introduction of large undissolved steel particles, inhomogeneously distributed, into the melt pool. These particles grew into large secondary phase islands giving the braze microstructure a relatively inhomogeneous and coarse appearance, as seen in sample 15 (Figure 4.10 a, b). By increasing β to 30°, the cooling rate of the melt pool decreased, which resulted in the complete melting and dissolving of the steel that was entering the melt pool from the top sheet. This resulted in the nucleation of small and well-dispersed Fe-Cu-Si precipitates within the Cu-matrix that resulted in significantly finer and relatively more homogeneous braze microstructure, as seen in sample 18 (Figure 4.10 c, d). The effect of this difference in morphology of particles/precipitates/dispersed IMC phase that results in the homogeneity and fineness of the braze bead microstructure is clearly shown by

the difference in joint strength and fracture mode between sample 15 (527 MPa, BB fracture) and sample 18 (588 MPa, HAZ fracture) (refer to Appendix B for further details). It is clear that the presence of inhomogeneously distributed, large Fe-rich secondary phase islands and a coarser braze microstructure has a detrimental effect on the strength of braze bead. The result is somewhat similar to what is observed during the overaging of precipitation-hardened alloys which results in the coarsening of the precipitates which lowers the overall strength of the alloy [72]. This suggests that the size and relative distribution of the Fe-Cu-Si particles in the braze microstructure has a significant effect on the mechanical properties of GMA-brazed joints. These results show that without the appropriate microstructural development within the braze bead, BB failure occurs regardless of the bead geometry due to the inherent weaknesses in the braze microstructure. Therefore, the formation of a finely-dispersed Fe-Cu-Si secondary phase with a relatively homogeneous distribution in the braze bead is required to improve the mechanical integrity of the braze microstructure, which subsequently increases the joint strength and shifts the fracture mode from BB to BM/HAZ.

4.4.4 Effect of torch position and angles on mechanical property

The effect of torch position and angles on the mechanical properties was observed using Figure 4.12. The effect of TP is clearly shown in Figure 4.12 (a) which shows that the TP of 0 mm resulted in superior joint properties regardless of the fracture mode due to a more balanced filler material deposition (relative to the top and bottom sheet) and a more even heat distribution across the joint geometry. Using the data from the samples tested when TP was set to 0 mm, the effect of torch angles (α and β) on the joint strength was represented using the 2D contour plot shown in Figure 4.12 (b), which shows that the joint strength increases when both α and β are increased. Based on the range of joint strength that each failure mode typically has, the contour plot was divided into 3 sections where the shift in failure mode going from IF→BB→BM/HAZ can be observed. Since the results have established that bead geometry itself does not have a significant direct influence on joint strength in GMAB applications, the aforementioned trend indicates that the difference in heat input, which is largely controlled by α and β, is the main controlling factor for joint strength

and the shift in failure mode. The results showed that as β increases, it promotes the formation of finely-dispersed Fe-Cu-Si precipitates with a relatively homogeneous distribution in the microstructure which strengthens the braze bead. When the strength of the braze bead exceeds the BM strength, the failure mode shifts from BB failure to BM/HAZ failure.

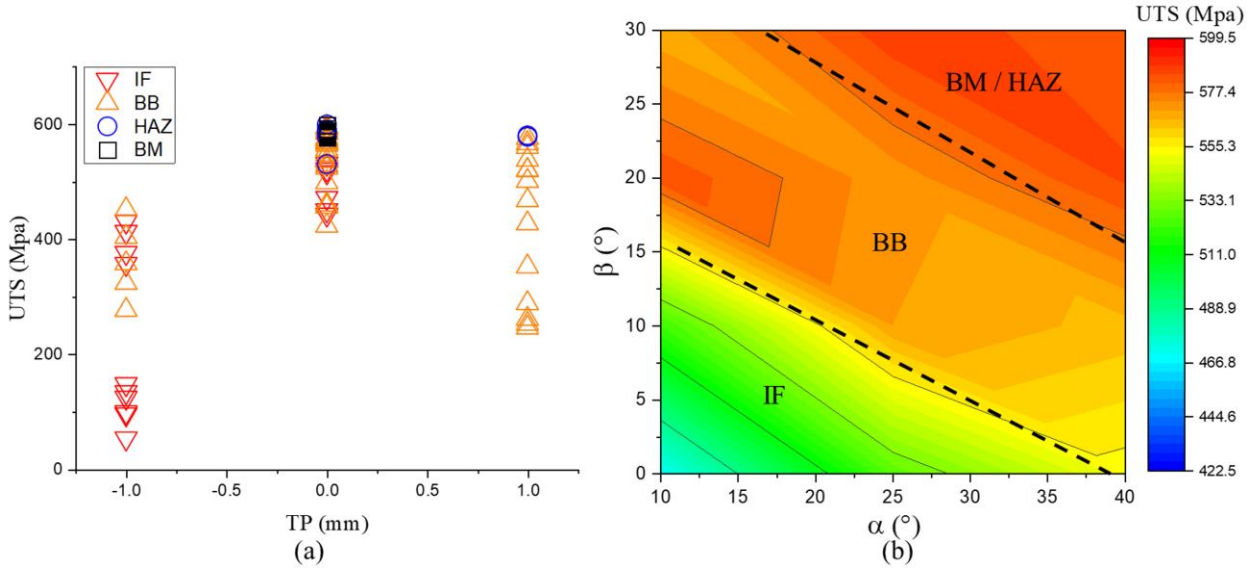

Figure 4.12: Effect of torch position and angles in mechanical property of the joint: (a) scatter plot showing the effect of TP, which shows that superior mechanical property is achieved when TP is at 0 mm; (b) 2D contour plot showing the effect of torch angles at TP of 0 mm, and it shows that increase in joint strength, as well as the shift of fracture mode, is observed with the increase of torch angles.

4.5 Summary

In this chapter, the effects of torch position and angles on the formation of the braze bead and the resulting geometry, the heat input distribution, and the mechanical properties of lap joints produced using GMAB of GA-coated DP600 were investigated. It was observed

that the arc and the droplet transfer behavior, along with the resulting bead geometry were sensitive to different changes in the torch position and angles. Several important key points are summarized as followings:

1. Increasing TP shifted the arc and the location of droplet transfer from the top sheet to the bottom sheet, increasing the L_1/W ratio that is taken as a measure of the bead geometry.
2. The work angle, α, has a similar effect to that of the TP but was observed to be less significant.
3. An increase in the push angle, β, promoted the formation of the melt pool ahead of the torch in the direction of travel and slowed down the cooling rate of the melt pool. This allowed for further spreading of the melt pool, increasing the width of the bead.
4. TP had a dominant effect on the bead geometry compared to the torch angles (α and β) because it was shown that TP controls both the location of the arc and the location of droplet transfer.
5. Torch position and angles can effectively control the heat input and its relative distribution into the workpiece, which has a significant effect on the formation of the HAZ.
6. The work angle can be used to effectively control the heat distribution between the top and bottom sheets, without any significant change in the bead geometry.
7. The homogeneity of the Fe-Si-Cu precipitates in the braze bead plays an important role in determining the mechanical properties of the joints:
    a. The results showed that large, inhomogeneously-distributed, undissolved Fe-rich secondary phase islands are formed in the braze microstructure when the substrates experienced a relatively lower heat input and a relatively higher cooling rate, which had a detrimental effect on the strength of the braze bead.
    b. The formation of finely-dispersed, homogeneously-distributed Fe-Cu-Si precipitates in the braze microstructure helped to strengthen the braze bead

which subsequently increased the joint strength and shifted the failure from BB to BM/HAZ.

8. The brazed joints made when the TP was set to 0 mm showed the most superior mechanical properties compared to when the TP was set to +1 mm and -1 mm, regardless of the fracture mode.
9. An increase in joint strength and a shift in the fracture mode from IF→BB→BM/HAZ was observed with an increase in the value of α and β due to the combinational effect of bead geometry, heat input distribution, and the final braze bead microstructure.

Chapter 5
Effect of gap clearance

For lap joint configuration, the presence of gap clearance between the overlapping sheets allows the molten filler material to enter the gap before solidification. The influence of gap clearance and wetting of filler material inside the gap is overlooked in the literature because the gap clearance has not been considered a factor of influence, as discussed in Chapter 2.6. In this chapter, the wetting of filler material in-between the base metal sheets, which is defined as 'root wetting' in this study, is investigated in two steps. First, the effect of gap clearance is analyzed experimentally by lap-shear tensile testing of 45 tensile samples with varying gap sizes from 0 mm to 1.6 mm. Second, the effect of the wetting behavior of molten filler material inside the gap is analyzed using plasma cleaning to control the wettability of the base metal surface prior to the GMAB experiments while keeping the gap size constant between 0.3–0.6 mm.

5.1 Effect of gap clearance

5.1.1 Measurements

The gap clearance and root wetting of each tensile coupon were measured prior to tensile testing, based on the measurements shown in Figure 5.1 which shows the typical cross-section of the GMA brazed sample, where *G* is the measured gap and *S* is the throat length, L_3 is wetting length at top, and L_4 is wetting length at bottom.

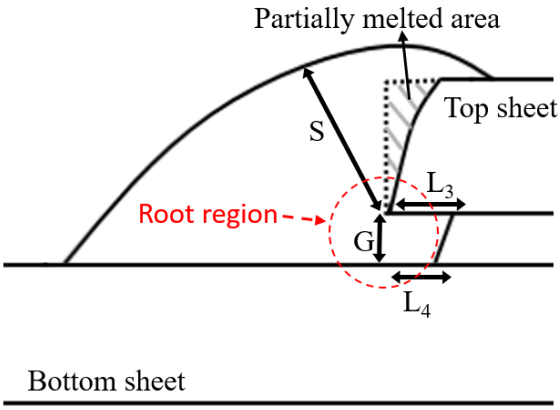

Figure 5.1: Schematic cross-section of a braze bead illustrating the measurements of gap size (G), wetting length at top sheet (L_3), and wetting length at bottom sheet (L_4); (c) tensile test coupon sample during lap-shear tensile testing. Obtained from Cho et al. [73]

5.1.2 The effect of gap clearance on joint strength

Figure 5.2 (a) shows that gap clearance has a significant effect on the mechanical properties of GMA brazed lap joints using GA DP600 base metal. The results showed that for the samples with no or little gap clearance, the deformation and the fracture occurred at a much lower load and elongation compared to the samples with a larger gap. As shown in Figure 5.2 (b), BB failure mode took place where the crack initiated at the root region, then propagated into the braze bead. As the gap size increases, the maximum load-bearing capacity of the joint increased until a gap size of about 0.6 mm. At this range, BM failure mode took place which showed 100% joint efficiency. Beyond 0.6 mm, the joint strength begins to deteriorate again. Figure 5.2 (d) and (e) show the crack path took place along the top sheet interface more as the joint strength further decrease. Figure 5.2 (f) shows the directly proportional relationship between gap size and total wetting length (L_3+L_4).

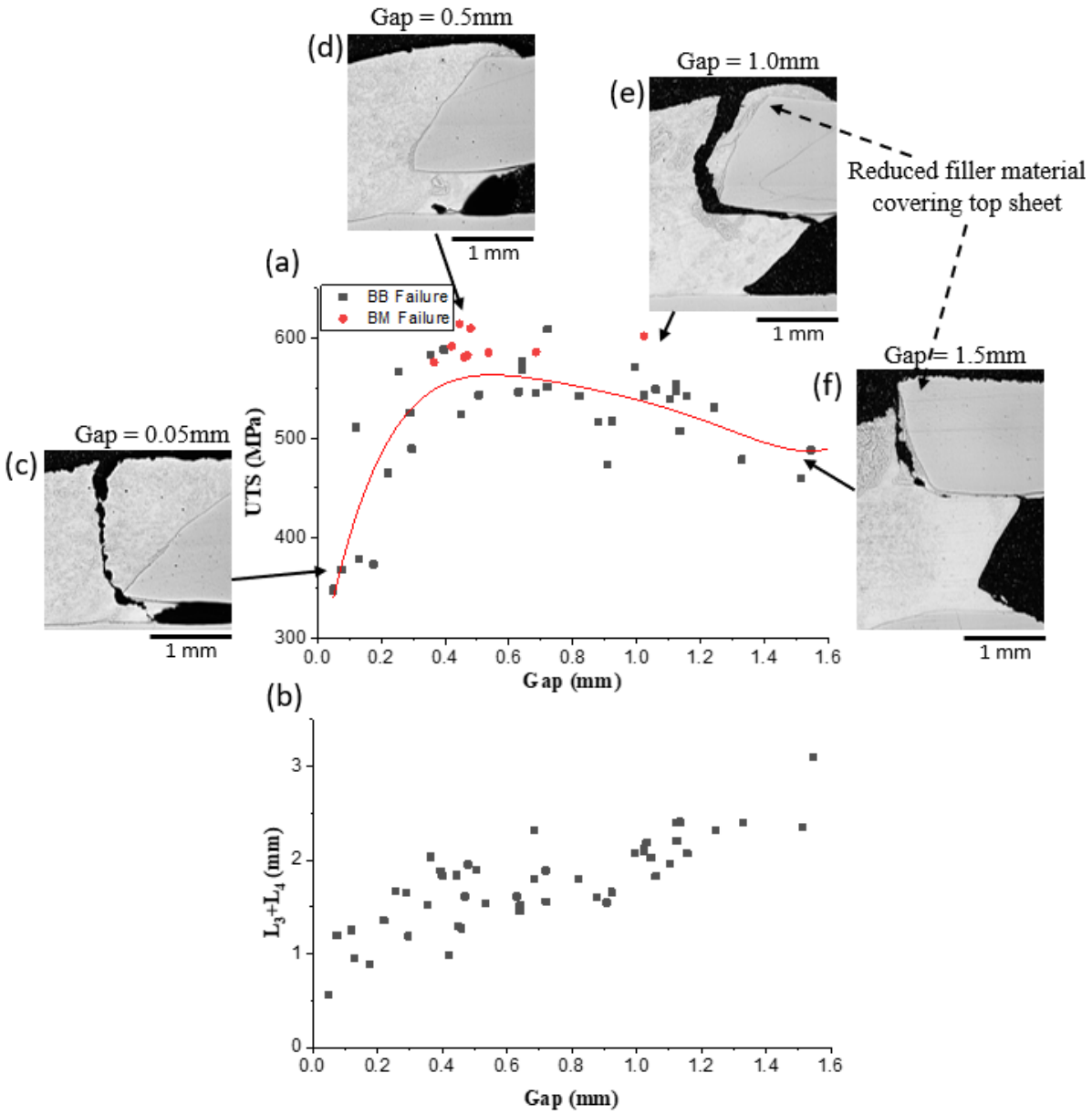

Figure 5.2: (a) Scatter plot showing the lap-shear tensile test result in ultimate tensile strength (UTS) with respect to the gap size; (b) scatter plot showing the effect of the gap in total wetting length (L_3+L_4); (c-f) cross-section of the fractured sample with the gap size of 0.05 mm, 0.5 mm, 1.0 mm, 1.5 mm respectively. Obtained from Cho et al. [73]

During lap-shear tensile testing, bending of the joint occurs at the root region due to the eccentricity of the load, causing a stress concentration to be developed at the root region [54]. The effect of this stress concentration on mechanical properties was captured by the DIC results in Figure 5.3 (a) showing a significantly lower strain before failure for the sample joint with a 0.05 mm gap compared to the sample with 0.45 mm gap, as shown in the typical load-displacement curve in Figure 5.3 (b).

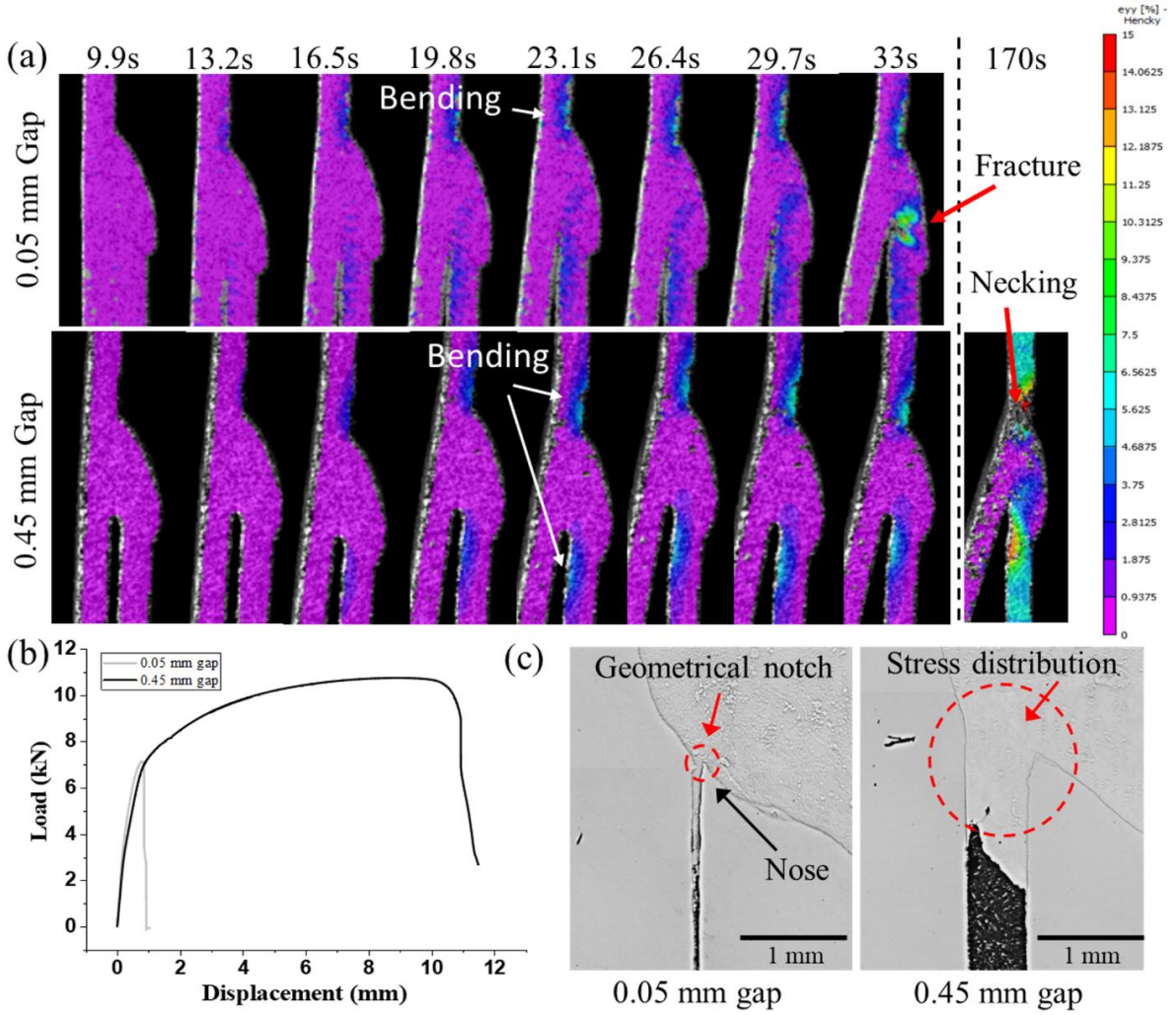

Figure 5.3: (a) images captured from DIC video of samples with a gap of 0.05 mm (upper) and 0.45 mm (lower). For the 0.05 mm gap sample, fracture occurs at 33s into the testing. For the 0.45 mm sample, necking at the base metal starts at 170 s into the

testing; (b) Typical load vs displacement curve showing the test sample with 0.05 mm gap and 0.45 mm gap; (c) cross-section of the braze bead showing the root area for the comparison of the amount of filler material wetting at root region depending on the gap size. Obtained from Cho et al. [73]

The presence of an optimal gap at the root had two effects: first, it decreased the geometrical notch effect on the braze bead which minimized the effect of the stress concentration, as shown in Figure 5.3 (c) [74]; second, it allowed for filler material to enter the gap which enabled the braze bead to 'hold' the top sheet in all 3 sides (Figure 5.2 c). This allowed the bending of the bottom sheet as well as the top sheet which helped the smooth transition of the load between the top and bottom sheets (indicated in Figure 5.3 a). These two combined effects significantly improved the mechanical properties of the joint as shown by the rapid increase of joint strength from 350 MPa to 600 MPa as the gap size increased from 0 mm and 0.4 mm (Figure 5.2 a).

Beyond the gap size of 0.6 mm, a gradual decrease in joint strength was due to two main reasons. Firstly, as the gap size increased beyond 0.6 mm, the amount of filler material covering the top sheet decreased (Figure 5.2 d and e), which decreased the throat size of the braze [28]. When the gap is further increased beyond 1 mm, the filler material no longer covers the top of the top sheet (Figure 5.2 e), which further reduces the length of interfacial bonding, decreasing the joint strength. Secondly, since the torch was aimed at the root where the filler material deposition occurred, the amount of heat distributed to the top sheet was reduced as the gap size increased which subsequently increased the distance between the top sheet and the heat source [75], This had a detrimental effect on the integrity of the interfacial bond between the braze and base metal due to the improper development of the intermetallic compound (IMC) layer at the interface [39]. This is shown by the fracture path of the failed samples which followed along the length of the IMC layer for the sample with a 1.5 mm gap size, as shown in Figure 5.2 (e).

5.2 Effect of root wetting

Under lap-shear tensile load, the failure at the braze bead would occur with a crack initiated at the root region propagating into the braze bead. Such failure mechanisms of GMA-brazed lap joint samples are commonly observed in the literature [37,39]. The root region, specifically the tip of the root wetting, was observed to vary in shape along the brazed seam. This profile of the root wetting was quantified from its cross-section by measuring the top wetting length (L_3) and bottom wetting length (L_4), and classified into 3 types as shown in Figure 5.4: type 1 is when the L_3 is equal to or greater than 2 times the L_4 (Figure 5.4 a), type 2 is when the L_3 is longer than the L_4 but less than 2 times (Figure 5.4 b), and type 3 is when the L_3 is equal to or less than the L_4 (Figure 5.4 c). Type 2 are commonly observed for the as-received condition.

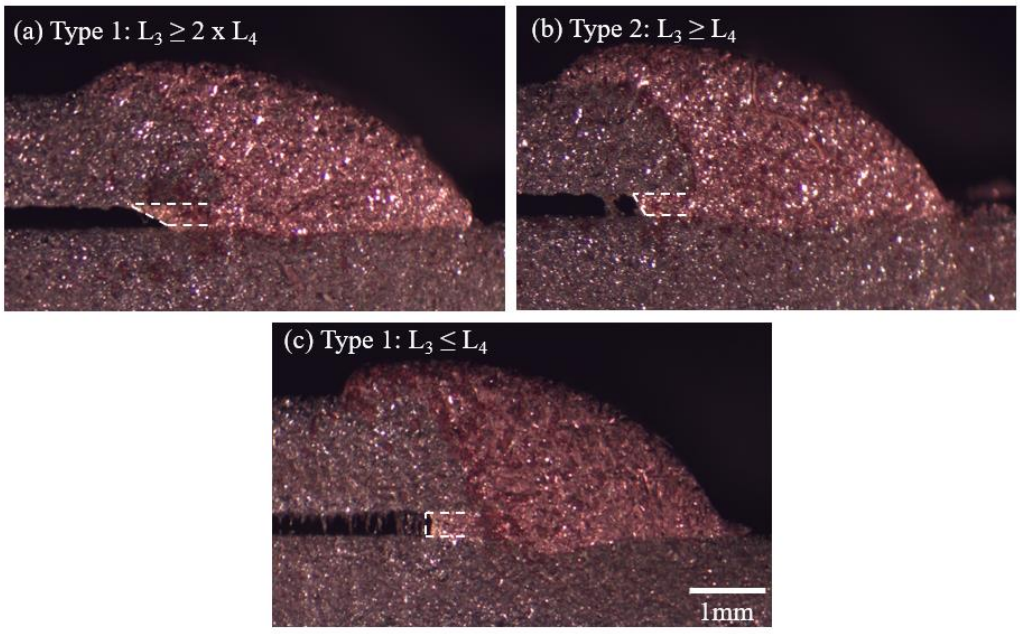

Figure 5.4: Stereoscope images of the brazed samples showing the root wetting profile: (a) Type 1, (b) Type 2, (c) Type 3

5.2.1 Root wetting profile control

To control the wetting profile of the brazed seam for experimental purpose, oxygen plasma-cleaning surface treatment is used to control the wettability of the base metal surface. The oxygen plasma cleaning technique uses ionized oxygen to remove any organic impurities (i.e., $C_xH_yO_z$) present on a surface of the material by the chemical reaction that forms by-products (i.e., $H_2O,\ CO_2$) which can then be easily removed way from the system [76]. Khan et al [50] has shown that the plasma cleaning increases the wettability of molten silicon bronze filler material on the Zn-coated steel sheets by increasing the surface free energy of the Zn-coating surface. The base metal samples were plasma cleaned in 3 conditions: plasma-cleaned top (PCT), plasma-cleaned bottom (PCB), and plasma-cleaned both top and bottom (PCTB), as shown in Figure 5.5 where the blue lines indicate the surface that was plasma-cleaned.

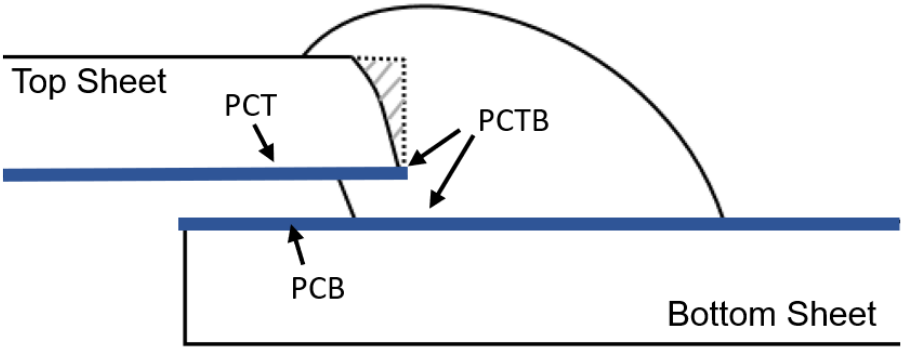

Figure 5.5: Schematic of a cross-section of braze bead illustrating each plasma cleaned conditions: plasma cleaned top (PCT), plasma cleaned bottom (PCB), and plasma cleaned top and bottom (PCTB).

Figure 5.6 shows the result of plasma cleaning for the wetting ratio. In general, PCT condition promoted type 1 wetting ratio, PCB condition promoted either type 1 or type 2

wetting ratio, and PCTB condition promoted type 3 wetting ratio as shown by the cross-section of the bead in Figure 5.6 (a-c). Figure 5.6 (d) clearly shows the effect of plasma cleaning compared to the as-received (AR) condition, where plasma cleaning either top or bottom surface increased the wetting ratio in general, but plasma cleaning both sides decreased the wetting ratio.

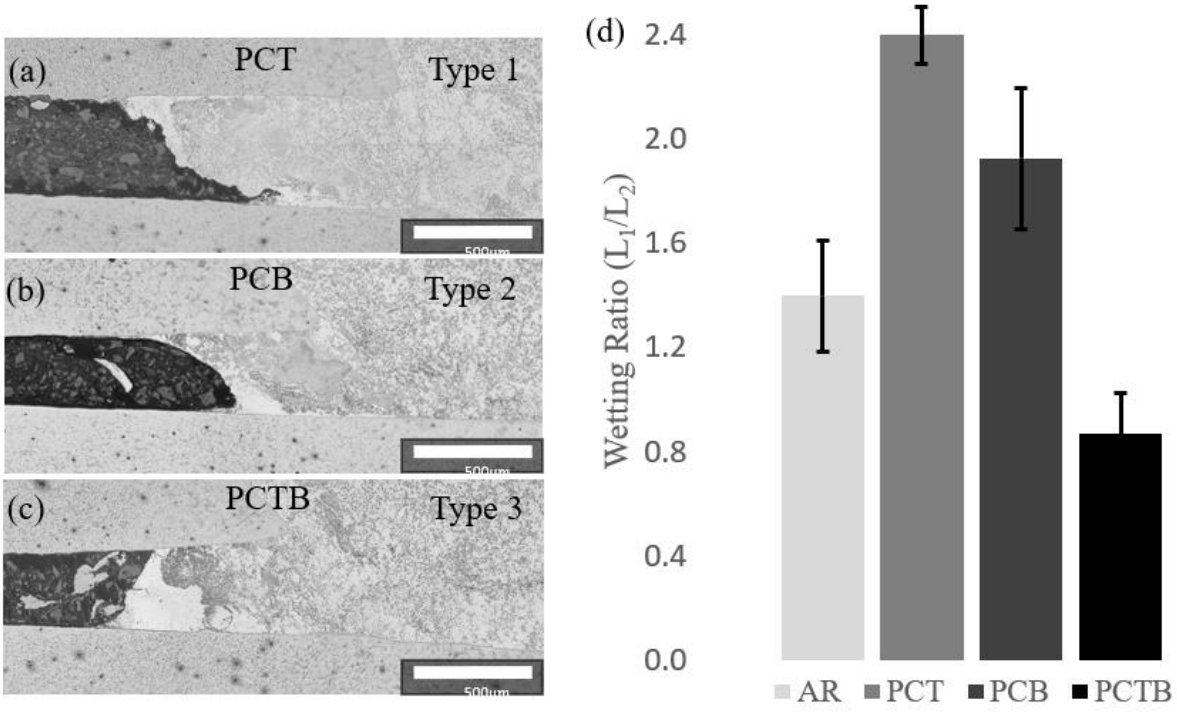

Figure 5.6: The result of plasma cleaning for each condition: (a) PCT condition promoted type 1 profile, (b) PCB condition promoted type 2 profile, (c) PCTB condition promoted type 3 profile, (d) wetting ratio observed for each plasma-cleaned condition. The arrows and dotted lines indicate the ZRA.

5.2.2 Effect of wetting profile on the fracture behavior

The root wetting profile was shown to have a significant effect on determining the fracture path as shown in Figure 5.9. For the type 1 profile, the crack initiated at the bottom

corner (red arrow). On the other hand, for the type 3 profile, the crack initiated at the top corner (yellow arrow). Although both samples failed at the braze bead, the type 1 sample was able to withstand 78.3 MPa more load than the type 3 sample. Such results suggests that the wetting profile controlled the weakest spot for crack formation which consequently affected the fracture path and joint strength. The fracture surface of the top sheet (Figure 5.7) shows the clear difference in fracture mechanics where the sample with the type 3 profile experienced interfacial fracture where the top sheet was 'peeled off' from the braze along the interface leaving a flat fracture surface behind (Figure 5.8 b). On the other hand, the sample with the type 1 wetting ratio left chunks of filler material on its fracture surface as the fracture path was along with the bottom sheet.

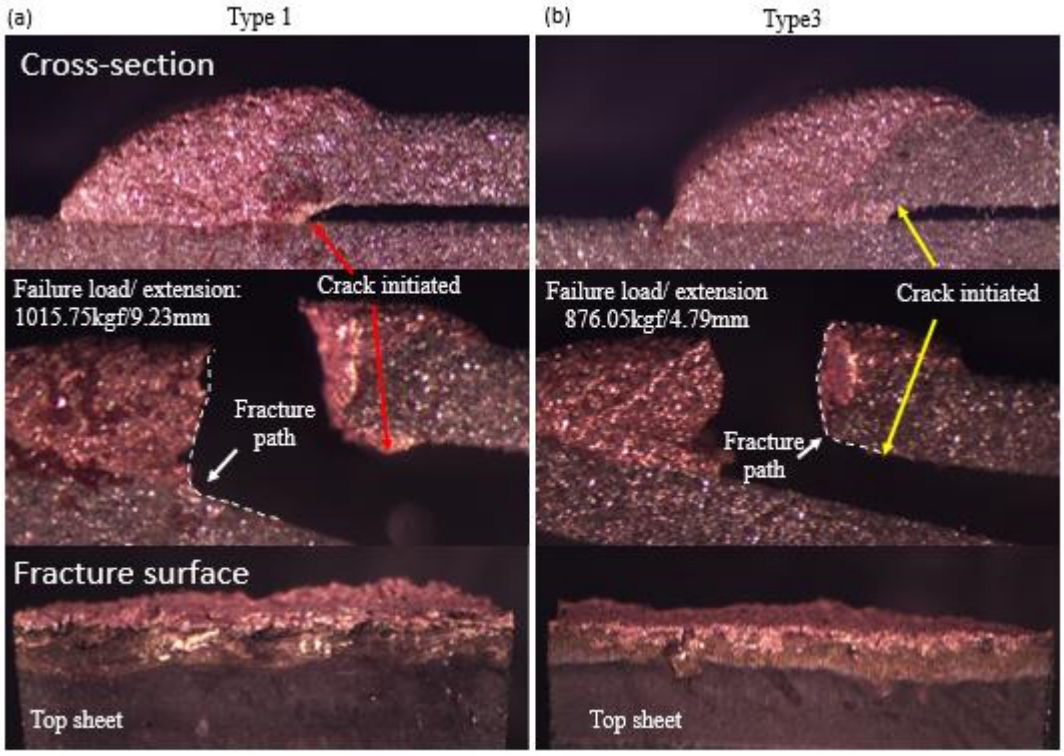

Figure 5.9: The comparison of failure mechanism between (a) Type 1 and (b) Type 2 root wetting profiles.

5.3 Effect of wetting profile on joint strength

12 samples with gap size between 0.3–0.5mm with varying wetting ratio from 0.5 to 2.5 were selected and tested under lap-shear tensile load. Figure 5.10 (a) shows the clear trend where joint strength is proportional to the wetting ratio. This is mainly due to the formation of stress concentration at the root region caused by the wetting profile. This is clearly shown by the DIC analysis in Figure 5.10 (b), where the type 3 profile sample showed large deformation in the braze bead and the stress concentration at the tip of the wetting on the top sheet in the root region immediately before fracture, indicated by the white arrow. On the other hand, the type 1 profile sample hardly showed any deformation in the braze bead at the same crosshead displacement as the type 3 profile sample. It can be deduced that the higher wetting profile promotes the smooth transition of the load which avoided the formation of the stress concentration at the root region of the bead.

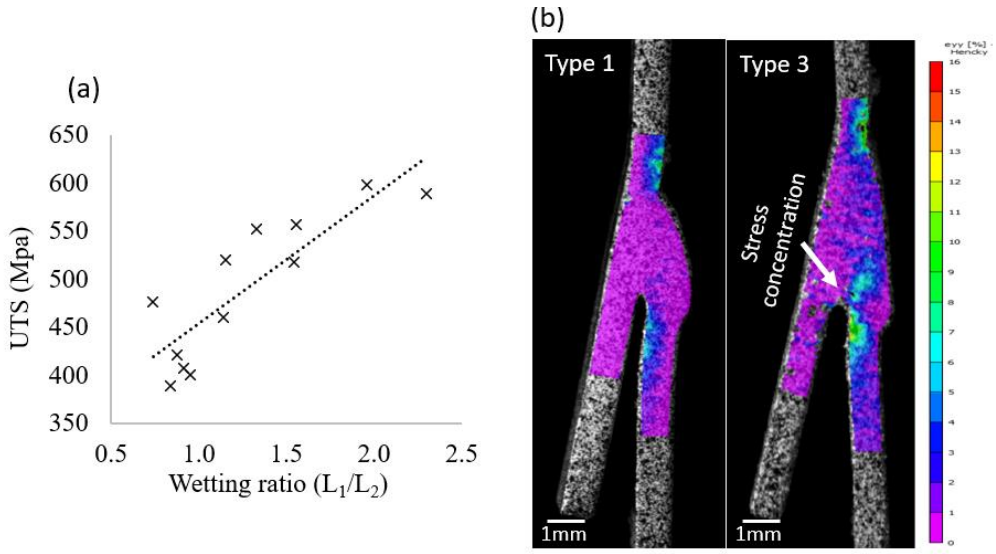

Figure 5.10: Lap-shear tensile test results for GMA brazed GA DP600 steel lap joint: (a) joint strength with respect to the wetting ratio, (b) DIC analysis result comparing the strain state between the samples with the type 1 and the type 3 wetting profile (both images are captured at the same crosshead displacement).

5.4 Summary

In this chapter, the effect of gap clearance of GMA brazed lap joints using GA DP600 steel and CuSi3Mn1 filler wire was investigated. It was shown that the gap clearance and wetting profile at the root region both have a large influence on the joint strength as they control the formation of stress concentration at the root region. The details of findings from this work can be summarized as followings.

1. Insufficient gap clearance has a detrimental effect on the mechanical properties of the joint due to a significant stress concentration present in the root region.
2. The optimal range of the gap clearance was found to be about 0.3–0.6 mm where 100% joint efficiency was achieved.
3. Beyond the 0.6 mm gap size, there was a gradual decrease in joint strength due to the decrease in the amount of brazing filler material covering the top sheet.
4. The wetting profile at the root region plays a large role in determining the joint strength as it affects the formation of a stress concentration by controlling the transfer of load between the top and bottom sheet.
5. A high wetting ratio (type 1) was beneficial for the joint strength as it allows for the smooth transition of load that avoids the formation of stress concentration at the root region.

Chapter 6

Effect of zinc-coating type

In Chapter 5, the effect of gap clearance and the wetting profile at the root region was investigated, and it was shown that the development of stress concentration at the root region was mainly responsible for the initiation of crack which was detrimental to the joint strength during a lap-shear tensile test. This suggests that the formation of a crack at the root region is critical for the mechanical property of the lap joint. In this chapter, the effect of Zn-coating type on weldability of the GMAB process is investigated by analyzing the microstructure of the root region of the GMA brazed samples in lap joint configuration using GI and GA-coated DP600 steel.

6.1 Microstructure of the root region

In the previous chapter, the root region of the GMA brazed lap joint was found to be the area of interest for the mechanical property of the joint as the stress concentration and the crack would always develop in this region under certain conditions such as no-gap condition and low wetting ratio. The typical microstructure of the root region is shown in Figure 6.1 (a). The microstructurally unique region was commonly observed near the outer edge of the braze material at the root indicated as the ‘white region’ in Figure 6.1 (a). The ‘white’ appearance of this region is mainly due to the absence of Fe-Si precipitates as shown in Figure 6.1. The EDX analysis for the chemical composition of the matrix and the precipitates for the entire region is shown in Figure 6.1 (b) and (c) respectively. For the matrix, the white region is composed of copper (72.9 wt%) and zinc (27.1 wt%), whereas no traces of zinc were found in the matrix of the darker region which contained a small percentage of iron (11.5 wt%) instead of zinc. The precipitates were found to be an intermetallic compound composed mainly of Si, Fe, and Cu elements. However, similar to the matrix, a small percentage of zinc (17.4 wt%) was found in the precipitates that were present in the white region, and no traces of zinc were found in these particles in the darker region. Therefore,

this white region, which has higher zinc content than other areas, can be considered as ZRA. It is clear to see that the zinc element plays a major role in the formation of different microstructural phases at the root region of the joints.

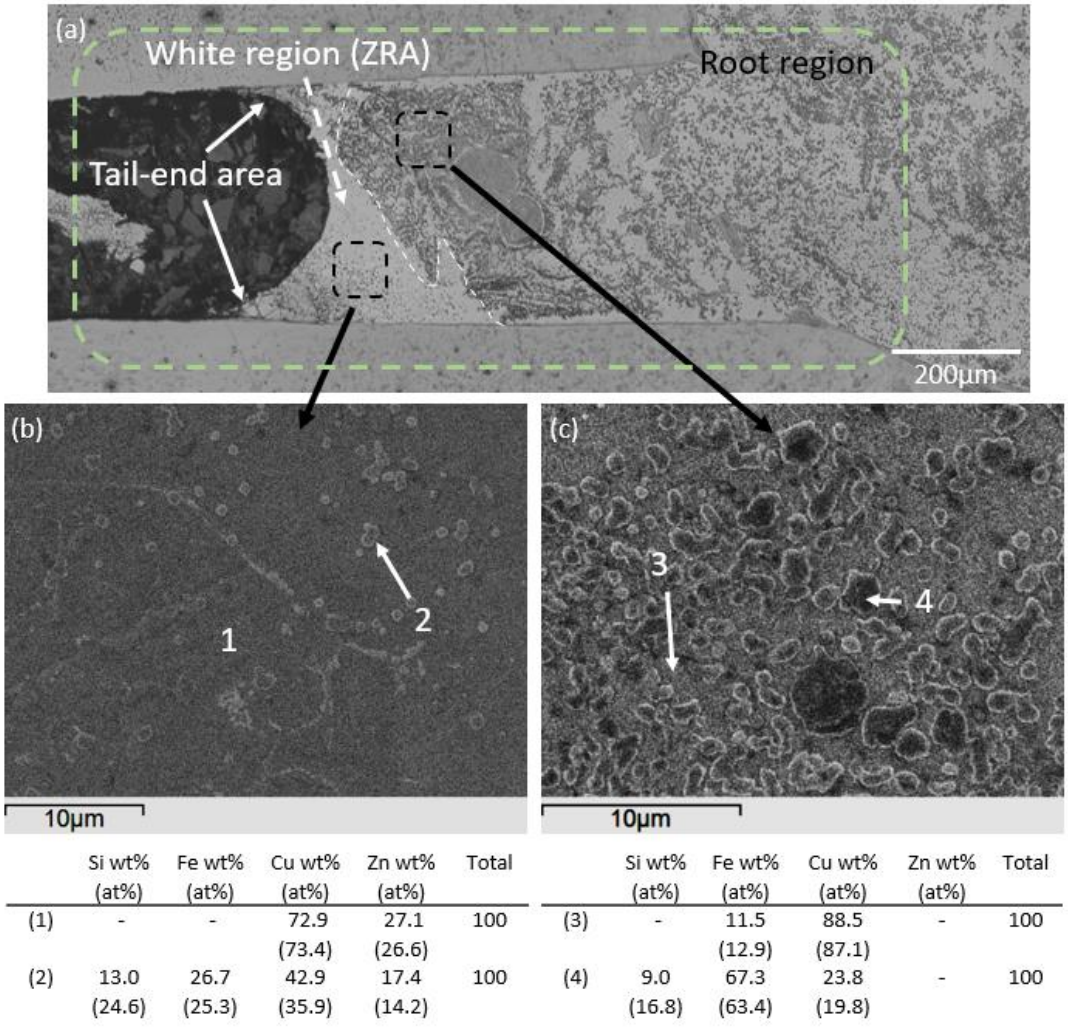

	Si wt% (at%)	Fe wt% (at%)	Cu wt% (at%)	Zn wt% (at%)	Total
(1)	-	-	72.9 (73.4)	27.1 (26.6)	100
(2)	13.0 (24.6)	26.7 (25.3)	42.9 (35.9)	17.4 (14.2)	100

	Si wt% (at%)	Fe wt% (at%)	Cu wt% (at%)	Zn wt% (at%)	Total
(3)	-	11.5 (12.9)	88.5 (87.1)	-	100
(4)	9.0 (16.8)	67.3 (63.4)	23.8 (19.8)	-	100

Figure 6.1: SEM and EDX analysis of the white region compared to the darker region observed from GMA brazing of GA DP600: (a) OM image of cross-sections showing the 'white region' and the darker region, (b) SEM image and EDX chemical analysis result of matrix and precipitate at the 'white region', (c) the same as (b) but at the darker region.

6.2 Effect of coating type on microstructure and chemistry

The elemental map shown in Figure 6.2 clearly shows the tailing-out effect of the ZRA, where the concentration of zinc increases towards the tail-end of the wetting. Reimann et al. [60], have reported that the formation of ZRA at the tip of the wetting is formed by the dissolution and accumulation of zinc at the outer edge of filler material during the wetting and spreading process of the molten filler material, which was also confirmed elsewhere in the literature [50,77]. The effect of different types of Zn-coating was shown by comparing the size of ZRA, where the GI-coated sample (Figure 6.2 a) was shown to have a much larger ZRA compared to that of the GA-coated sample (Figure 6.2 b). This variance in the alloying chemistry of this region must be attributed primarily to the GI-coating being almost pure zinc (~99 wt.% Zn), whereas the GA-coating contains about 10 wt.% Fe (Table 3.1).

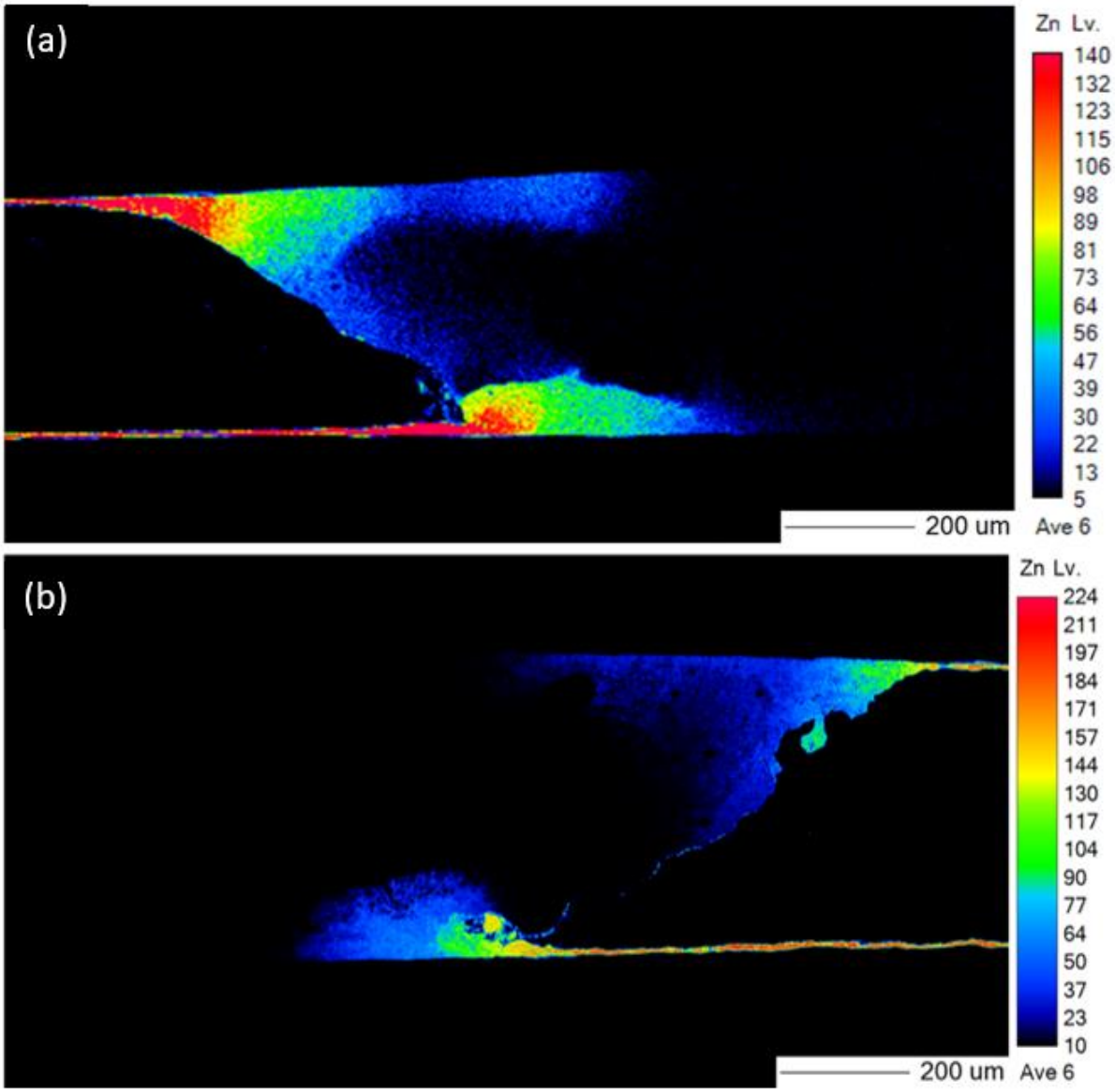

Figure 6.2: Elemental maps of the root region of the GI-coated and GA-coated brazed joints for Zn: (a) GI-coated sample, (b) GA-coated sample. Note that the color scale used is different for each coating since it was chosen for the best visibility of the element. Obtained from Khan et al [78]**.**

As a result of different Zn-coating chemistry, the microstructure and alloying composition of the tail-end region of the root area were found to be significantly different. EDX analysis of the matrix and precipitates in this region for the GI and GA-coated samples are shown in Figure 6.3 (a) and (b), respectively. The matrix consisted of mainly copper and zinc for both coatings. However, the GI-coated sample showed a significantly higher zinc content of about 40-50 wt.%, while the GA-coated sample had about 30 wt.% zinc. A similar trend was observed for the precipitates, such that the 26.1 wt.% and 17.1 wt.% of zinc was found for GI and GA coated samples respectively.

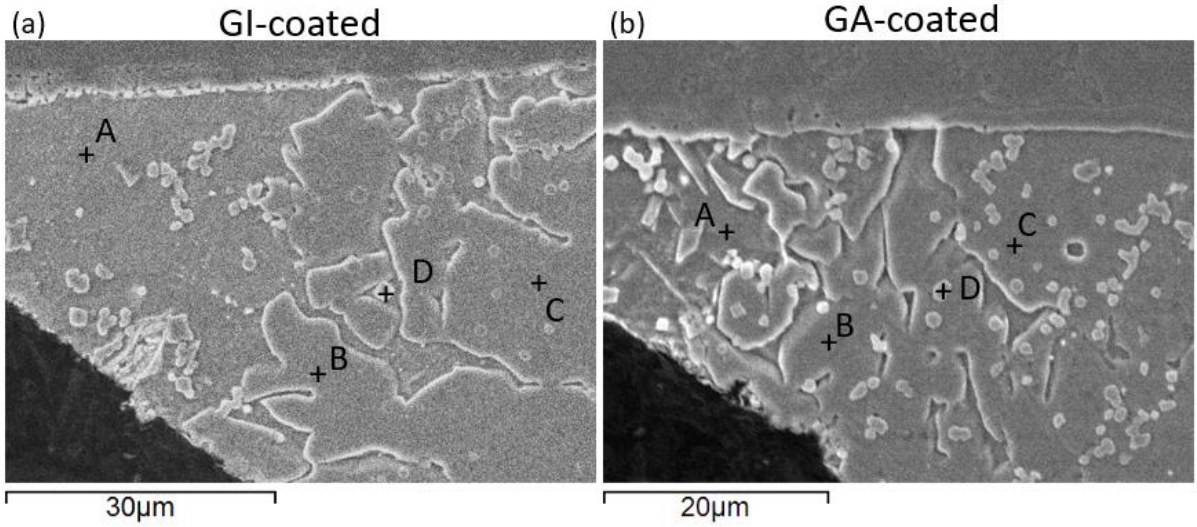

Spectrum	Si	Fe	Cu	Zn	Total
A			47.4	52.6	100
B			56.8	43.2	100
C			65.2	34.8	100
D	7.2	37.8	28.8	26.1	100

Spectrum	Si	Fe	Cu	Zn	Total
A			53.4	46.6	100
B		3.0	59.4	37.7	100
C			66.9	33.1	100
D	11.3	40.0	31.6	17.1	100

Figure 6.3: EDX analysis performed on the tail-end of the root region: (a) chemical composition (all in wt.%) of different phases of the matrix (point A, B, C) and precipitate (point D) for GI-coated sample, (b) same EDX analysis for GA-coated sample.

The IMC layer at the tail-end region was also observed to be different for GI and GA coated samples. For GI coated samples, the non-homogeneous microstructurally different

interfacial IMC layer was observed at the tail-end area, as indicated in Figure 6.4 (a). For the GA-coated samples, the IMC layer was observed to be consistent till the very end of the tail, as shown in Figure 6.4 (b). This could be attributed to the GA-coating having a higher Fe concentration which aids the development of the IMC layer which is consisted of Fe, Si, and Cu [46,50]. In addition, the pre-existing crack was often found at the tail-end for GI-coated samples, as indicated in Figure 6.4 (a).

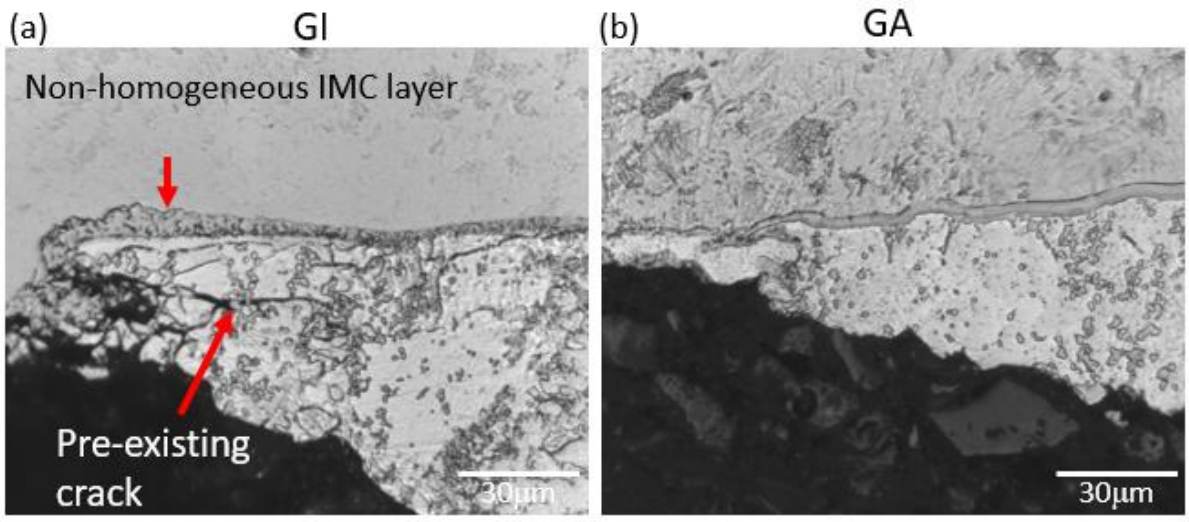

Figure 6.4: Typical tail-end area of the ZRA for each Zn-coating type: (a) GI-coated sample, (b) GA-coated sample.

6.3 Mechanical property

6.3.1 Hardness

The effect of zinc content on the mechanical property of the tail-end region was evaluated using Vickers hardness testing. Figure 6.5 shows the hardness results of individual indents. The average hardness of the tail-end region in ZRA for GI and GA-coated samples were found to be 434 HV and 187 HV respectively, which is significantly different. This is attributed to the role of zinc concentration on the Cu-Zn compound. Freudenberger et al.

[79], reported that the Cu-Zn compound exhibits near 0% strain to failure when zinc concentration is higher than 40 wt.%, which indicates that the compound is extremely brittle. Then, the strain to failure increases rapidly with the decrease of Zn concentration where the maximum strain to failure of 60% is observed when the zinc concentration is about 25-30 wt.%. Therefore, the concentration of zinc determines the mechanical property of ZRA, and this is the reason for the higher hardness observed for the GI-coated samples compared to the GA-coated samples. This also explains the pre-existing crack observed in Figure 6.4 (a) which could have been developed during solidification, or even from the grinding and polishing during the sample preparation due to its extreme brittleness.

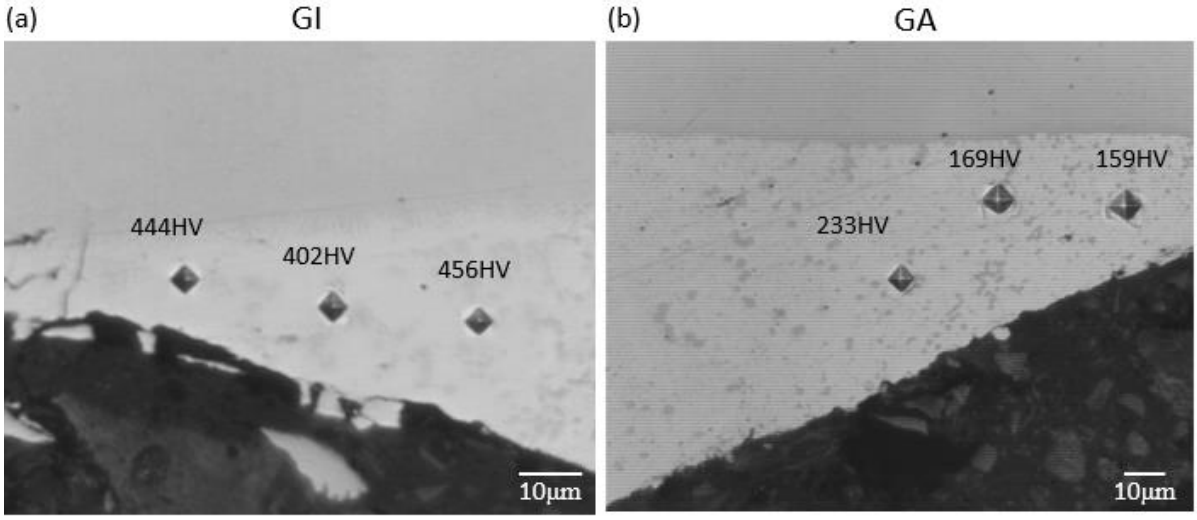

Figure 6.5: Hardness measured at the ZRA for each coating type: (a) GI-coated sample, (b) GA-coated sample.

6.3.2 Joint strength

Figure 6.6 (a) shows the average UTS results for the GI and GA-coated samples. The sample size of 8 is used per each type of Zn-coating, which are GMA brazed under the same conditions. To reasonably filter out the effect of the wetting ratio, only the samples with the type 2 wetting profile are chosen for the lap-shear tensile test. It is clear that the GA-coated

samples have superior joint strength compared to the GI-coated samples. In addition, all GI-coated samples had the fracture path along with the top interface (Figure 6.6 b), which is similar to the type 3 wetting profile for GA-coated samples shown in Figure 5.9. The weaker joint strength of GI-coated sample is most likely to be due to the brittle nature of the ZRA which caused pre-existing cracks and non-homogeneous IMC layer. Under the lap-shear tensile load, the crack forms readily at the tail-end of ZRA along with the top sheet interface, then the crack propagates along with the non-homogeneous IMC layer. As a result, the top sheet 'peels off' from the braze bead due to the peeling stress that acts on the root region.

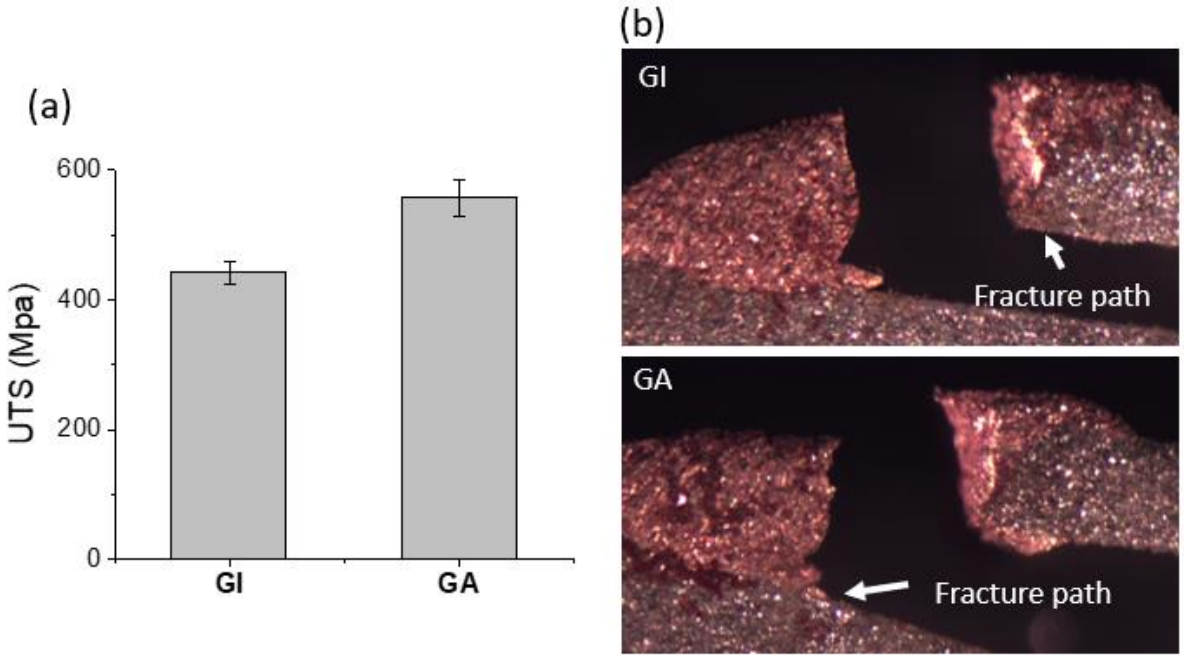

Figure 6.6: Comparison of GI and GA-coated samples under lap-shear tensile testing: (a) average UTS result (95% confidence level error bar). The sample size of 8 is used to calculate the average for each coating type, and all samples are GMA brazed under the same process conditions and have the wetting ratio between 1–1.6. (b) Typical fracture path observed for GI and GA-coated samples.

6.3.3 Summary

In this chapter, the effect of GI and GA-coating type on mechanical properties of GMA brazed lap joint has been investigated. It was shown that GI and GA-coating type plays a significant role in determining the joint strength due to the difference in alloying chemistry at the ZRA in the root region. The details of findings from this work can be summarized as followings.

1. GI-coating has a detrimental effect on joint strength due to the high Zn concentration at the tail-end of the root region that forms Cu-Zn alloy with extremely high brittleness.
2. Due to the lower Fe concentration of GI-coating, the IMC layer at the tail-end region is underdeveloped, which increases the crack susceptibility in this region.
3. GA-coated samples have superior joint strength in general compared to GI-coated samples as it forms a much more ductile Cu-Zn alloy at the ZRA and fully developed IMC layer, which is attributed to the GA-coating chemistry that has lower zinc concentration and higher Fe concentrations.

Chapter 7
Conclusion

The objective of this thesis was to further optimize the GMAB process by investigating some of the critical factors that were influencing the mechanical properties of GMA brazed lap joint based on the experimental work performed. The critical factors investigated in this thesis were the torch angle and position, the gap clearance, and the coating type (GI and GA-coatings), which are the topics discussed in Chapters 4, 5, and 6 respectively. This chapter draws conclusions from Chapters 4, 5, and 6, then proposes future work to be done to further optimization of the GMAB process.

7.1 Effect of torch angle and position

The investigation of the effect of torch angle and position during the GMAB process is experimentally approached using high-speed imaging to capture the behavior of arc and the droplet transfer which was then directly correlated to the resulting bead geometry, heat distribution, and mechanical properties of the joint. The results showed that the position of the torch had a dominant effect over the torch angles for the bead geometry and heat distribution as the torch position directly controlled the location of arc and droplet transfer which are the main source of heat input. It was shown that the torch position at the center of the root (TP = 0 mm) resulted in the superior mechanical property over any other positions, regardless of the fracture mode. The work angle had a similar effect as the torch position in terms of arc behavior, where increasing the work angle shifted the arc towards the bottom sheet. Consequently, the work angle effectively controlled the heat distribution between the top and bottom sheets without changing the bead geometry significantly. The push angle had a significant effect on molten pool behavior where the increase in push angle promoted the spreading of the molten pool by ‘pushing’ the molten pool ahead of the torch in the travel direction. Furthermore, an increase in push angle decreased the cooling rate of the melt pool which promoted the formation of finely dispersed and homogeneously distributed Fe-Cu-Si

precipitates throughout the braze bead which subsequently increased the mechanical properties of the joint. As a result, an increase in torch angles improved the mechanical properties of the lap joint.

7.2 Effect of gap clearance

The effect of gap clearance on mechanical properties of GMA brazed lap joint is investigated experimentally. The results showed that 0.3–0.6 mm of gap size resulted in optimal mechanical properties of the lap joint. This is mostly attributed to the formation of stress concentration at the root region due to the eccentricity of the load during lap-shear tensile testing, which is the most severe under the insufficient gap size. This effect of stress concentration is reduced as the gap size increase to the optimal range, rapidly increasing joint strength. In addition, the wetting behavior of molten filler material in the gap was also found to be influential for the mechanical properties of the joint. The increase of wetting ratio (L_1/L_2) promoted the smooth transition of load between the top and bottom sheet which avoided the formation of stress concentration at the root region, and improved the mechanical properties of the joint.

7.3 Effect of zinc-coating type

The effect of GI and GA-coating type on mechanical properties of GMA brazed lap joint has been investigated. It was shown that the GA-coating results in superior joint properties than GI-coating in general. This is attributed to the difference in mechanical property of ZRA at the tail-end region in the root region. Due to the higher zinc concentration of GI-coating, extremely brittle Cu-Zn alloy is formed at the tail-end region which increases crack susceptibility. Also, the IMC layer in this region is developed improperly due to the low Fe content of the GI-coating. On the other hand, a much more ductile Cu-Zn alloy and properly developed IMC layer is observed for GA-coating due to its lower zinc and higher Fe content. Therefore, GA-coated steels are more appropriate for the GMAB process using Si-bronze filler material.

7.4 Recommended future work

Based on the present work, the following recommendations are proposed to further optimize the GMAB process.

1. The experimental work for the investigation of the effect of torch angle and position was performed in a horizontal position (2F) only. A similar experiment can be performed on other positions (i.e., vertical position (3F)) to further expand the application of GMAB in the manufacturing process.
2. The control of gap size remains a challenge as it is very difficult to control the gap size precisely under 1 mm in real-life industrial applications. Moreover, the GMAB process is typically used to join long sheets of steel together in the automotive industry (i.e., root panel, trunk panel). Therefore, further mechanical testing using steel sheets and the development of a gap control method are suggested to verify the application of gap size control in the industrial setting.
3. There are various zinc coating types beyond GI and GA. Additional GMAB experiments can be performed using various coatings and base metals to explore the ‘brazability’ using the GMAB process.

References

[1] C. Lesch, N. Kwiaton, F.B. Klose, Advanced High Strength Steels (AHSS) for Automotive Applications − Tailored Properties by Smart Microstructural Adjustments, Steel Res. Int. 88 (2017) 1–21. https://doi.org/10.1002/srin.201700210.

[2] M.S. Khan, M.H. Razmpoosh, E. Biro, Y. Zhou, A review on the laser welding of coated 22MnB5 press-hardened steel and its impact on the production of tailor-welded blanks, Sci. Technol. Weld. Join. 25 (2020) 447–467. https://doi.org/10.1080/13621718.2020.1742472.

[3] M. Shehryar Khan, A. Macwan, E. Biro, Y. Zhou, α-ferrite Suppression during Fiber Laser Welding of Al-Si Coated 22MnB5 Press-Hardened Steel, Weld. J. 100 (2021). https://doi.org/10.29391/2021.100.018.

[4] M. Shehryar Khan, M.H. Razmpoosh, A. Macwan, E. Biro, Y. Zhou, Optimizing weld morphology and mechanical properties of laser welded Al-Si coated 22MnB5 by surface application of colloidal graphite, J. Mater. Process. Technol. 293 (2021) 117093. https://doi.org/10.1016/j.jmatprotec.2021.117093.

[5] X. Li, S. Lawson, Y. Zhou, F. Goodwin, Novel technique for laser lap welding of zinc coated sheet steels, J. Laser Appl. 19 (2007) 259–264. https://doi.org/10.2351/1.2795755.

[6] S. Kimura, S. Takemura, M. Mizutani, S. Katayama, Laser brazing phenomena of galvanized steel and pit formation mechanism, ICALEO 2006 - 25th Int. Congr. Appl. Laser Electro-Optics, Congr. Proc. 528 (2006). https://doi.org/10.2351/1.5060939.

[7] M. Shehryar Khan, P. Enrique, A. Ghatei-Kalashami, J.G. Lopes, N. Schell, J.P. Oliveira, E. Biro, Y. Norman Zhou, The influence of in-situ alloying of electro-spark deposited coatings on the multiscale morphological and mechanical properties of laser welded Al–Si coated 22MnB5, Mater. Sci. Eng. A. 839 (2022) 142830. https://doi.org/10.1016/j.msea.2022.142830.

[8] M.S. Khan, S. Ali, D. Westerbaan, W. Duley, E. Biro, Y.N. Zhou, The effect of laser impingement angle on the optimization of melt pool geometry to improve process stability during high-speed laser welding of thin-gauge automotive steels, J. Manuf. Process. 78 (2022) 242–253. https://doi.org/10.1016/j.jmapro.2022.04.022.

[9] M. Shehryar Khan, S.I. Shahabad, M. Yavuz, W.W. Duley, E. Biro, Y. Zhou, Numerical modelling and experimental validation of the effect of laser beam defocusing on process optimization during fiber laser welding of automotive press-hardened steels, J. Manuf. Process. 67 (2021) 535–544. https://doi.org/10.1016/j.jmapro.2021.05.006.

[10] R. Sa-nguanmoo, E. Nisaratanaporn, Y. Boonyongmaneerat, Hot-dip galvanization with pulse-electrodeposited nickel pre-coatings, Corros. Sci. 53 (2011) 122–126. https://doi.org/10.1016/j.corsci.2010.09.031.

[11] S.M.A. Shibli, B.N. Meena, R. Remya, A review on recent approaches in the field of hot dip zinc galvanizing process, Surf. Coatings Technol. 262 (2015) 210–215. https://doi.org/10.1016/j.surfcoat.2014.12.054.

[12] L. Dosdat, J. Petitjean, T. Vietoris, O. Clauzeau, Corrosion resistance of different metallic coatings on press-hardened steels for automotive, Steel Res. Int. 82 (2011) 726–733. https://doi.org/10.1002/srin.201000291.

[13] C. Chovet, S. Guiheux, Possibilities offered by MIG and TIG brazing of galvanized ultra high strength steels for automotive applications, Metall. Ital. 98 (2006) 47–54.

[14] M.H. Razmpoosh, A. Macwan, E. Biro, D.L. Chen, Y. Peng, F. Goodwin, Y. Zhou, Liquid metal embrittlement in laser beam welding of Zn-coated 22MnB5 steel, Mater. Des. 155 (2018) 375–383. https://doi.org/10.1016/j.matdes.2018.05.065.

[15] H. Kang, L. Cho, C. Lee, B.C. De Cooman, Zn Penetration in Liquid Metal Embrittled TWIP Steel, Metall. Mater. Trans. A Phys. Metall. Mater. Sci. 47 (2016) 2885–2905. https://doi.org/10.1007/s11661-016-3475-x.

[16] Y.G. Kim, I.J. Kim, J.S. Kim, Y. Il Chung, D.Y. Choi, Evaluation of Surface Crack in Resistance Spot Welds of Zn-Coated Steel, Mater. Trans. 55 (2014) 171–175. https://doi.org/10.2320/matertrans.M2013244.

[17] L. Cho, H. Kang, C. Lee, B.C. De Cooman, Microstructure of liquid metal embrittlement cracks on Zn-coated 22MnB5 press-hardened steel, Scr. Mater. 90 (2014) 25–28. https://doi.org/10.1016/j.scriptamat.2014.07.008.

[18] A. Ghatei-Kalashami, M.S. Khan, M.Y. Lee, Y.N. Zhou, High-temperature phase evolution of the ZnAlMg coating and its effect on mitigating liquid-metal-embrittlement cracking, Acta Mater. 229 (2022) 117836. https://doi.org/10.1016/j.actamat.2022.117836.

[19] C. Morano, R. Tao, M. Alfano, G. Lubineau, Effect of Mechanical Pretreatments on Damage Mechanisms and Fracture Toughness in CFRP/Epoxy Joints, Materials (Basel). 14 (2021). https://doi.org/10.3390/ma14061512.

[20] H. Zhao, X. Duan, M. Ma, L. Lu, Z. Cai, P.C. Wang, J.D. Fickes, Dynamic characteristics of adhesive bonded high strength steel joints, Sci. Technol. Weld. Join. 15 (2010) 486–490. https://doi.org/10.1179/136217110X12714217309731.

[21] C. Morano, F. Musiari, F. Moroni, G.D. Spennacchio, D. Di Lonardo, M. Alfano, Experimental analysis of steel joints bonded with automotive grade hot setting structural adhesives, Proc. Inst. Mech. Eng. Part L J. Mater. Des. Appl. 233 (2019) 2084–2093. https://doi.org/10.1177/1464420718817860.

[22] J. Singh, K.S. Arora, N. Shajan, M. Shome, D.K. Shukla, Influence of Novel Torch Type on Mechanical and Microstructural Characteristics of Cold Metal Transfer Brazed Joints, J. Manuf. Sci. Eng. 143 (2021). https://doi.org/10.1115/1.4047735.

[23] M. Mohammadpour, B. Yang, H.P. Wang, J. Forrest, M. Poss, B. Carlson, R. Kovacevic, Influence of laser beam inclination angle on galvanized steel laser braze quality, Opt. Laser Technol. 129 (2020) 106303. https://doi.org/10.1016/j.optlastec.2020.106303.

[24] K. Weman, Welding Processes Handbook, Woodhead publishing Ltd, 2003. http://www.sciencedirect.com/science/article/pii/B9780857095107500227.

[25] P. Andreazza, A. Gericke, K.M. Henkel, Investigations on arc brazing for galvanized heavy steel plates in steel and shipbuilding, Weld. World. 65 (2021) 1199–1210. https://doi.org/10.1007/s40194-021-01087-2.

[26] Y. Kim, K. Park, S. Kwak, A review of arc brazing process and its application in automotive, Int. J. Mech. Eng. Robot. Res. 5 (2016) 246–250. https://doi.org/10.18178/ijmerr.5.4.246-250.

[27] S. Basak, H. Das, T.K. Pal, M. Shome, Corrosion Behavior of MIG Brazed and MIG Welded Joints of Automotive DP600-GI Steel Sheet, J. Mater. Eng. Perform. 25 (2016) 5238–5251. https://doi.org/10.1007/s11665-016-2356-1.

[28] K. Weman, C. Johansson, Welding Processes Handbook, 2012.

[29] N. Baluch, Z.M. Udin, C.S. Abdullah, Advanced High Strength Steel in Auto Industry: an Overview, Eng. Technol. Appl. Sci. Res. 4 (2014) 686–689. https://doi.org/10.48084/etasr.444.

[30] AHSS Application guidelines, A new global formability diagram, (2021). https://ahssinsights.org/blog/a-new-global-formability-diagram/ (accessed January 24, 2022).

[31] A.R. Marder, The Metallurgy of Zinc-Coated Steel, Prog. Mater. Sci. 45 (2000) 191–271. https://doi.org/10.1038/089315a0.

[32] S. Dionne, The characterization of continuous hot-dip galvanized and galvannealed steels, JOM. 58 (2006) 32–40. https://doi.org/10.1007/s11837-006-0157-y.

[33] F.E. Goodwin, Developments in the production of galvannealed steel for automotive, Trans. Indian Inst. Met. 66 (2013) 671–676. https://doi.org/10.1007/s12666-013-0290-6.

[34] M. Autio, P. Belanger, F. Cheng, A. Desai, S. Dinda, M. Fistler, R. Johnson, D.

Kelley, T. Klix, D. Nielson, G. Patria, R. Dave, J. Rozenbaum, J. Siekirk, M. Stephens, R. Traficante, Galvanneal (GA) vs . Galvanized (GI) Steels, 2006. https://doi.org/10.13140/RG.2.2.13435.36641.

[35] SDI steel dynamics, The galvanizing process, (n.d.). https://www.steeldynamics.com/The-Techs/Products/Process-Overview.aspx.

[36] H.S. Horst Albrecht, Gerd Klein, Klaus Pesler, Method for arc brazing using an inert gas, WO2000024545A1, 1999.

[37] S. Basak, T.K. Pal, M. Shome, High-cycle fatigue behavior of MIG brazed galvanized DP600 steel sheet joint—effect of process parameters, Int. J. Adv. Manuf. Technol. 82 (2016) 1197–1211. https://doi.org/10.1007/s00170-015-7451-1.

[38] I. Acar, V. Siksik, F. Varol, S. Aslanlar, Investigation of mechanical properties of butt joints of DP800 thin zinc-coated steel plates, cmt-brazed using different current intensities, Acta Phys. Pol. A. 132 (2017) 849–851. https://doi.org/10.12693/APhysPolA.132.849.

[39] J. Singh, K. Singh Arora, N. Shajan, D.K. Shukla, M. Shome, Role of bead shape and dispersed intermetallic phases in determining the strength of CMT brazed DP780 lap joints, J. Manuf. Process. 44 (2019) 207–215. https://doi.org/10.1016/j.jmapro.2019.06.007.

[40] S.J. Lee, A. Sharma, D.H. Jung, J.P. Jung, Influence of arc brazing parameters on microstructure and joint properties of electro-galvanized steel, Metals (Basel). 9 (2019). https://doi.org/10.3390/met9091006.

[41] J. Li, H. Li, H. Wei, Y. Gao, Effect of torch position and angle on welding quality and welding process stability in Pulse on Pulse MIG welding–brazing of aluminum alloy to stainless steel, Int. J. Adv. Manuf. Technol. 84 (2016) 705–716. https://doi.org/10.1007/s00170-015-7734-6.

[42] S. Jaypuria, T.R. Mahapatra, S. Sahoo, O. Jaypuria, Effect of arc length trim and

adaptive pulsed-MIG process parameters on bead profile of stainless steel with synergic power source, Mater. Today Proc. 26 (2019) 787–795. https://doi.org/10.1016/j.matpr.2020.01.027.

[43] A. O'Brien, K. Sinnes, Welding Handbook, Volume 5 - Materials and Applications, Part 2 (9th Edition), 2015. https://app.knovel.com/web/toc.v/cid:kpWHVMAP13/viewerType:toc/root_slug:welding-handbook-volume-5---materials-and-applications-part-2-9th-edition.

[44] P. Makwana, S.F. Goecke, A. De, Real-time heat input monitoring towards robust GMA brazing, Sci. Technol. Weld. Join. 24 (2019) 16–26. https://doi.org/10.1080/13621718.2018.1470290.

[45] D.R. Askeland, P.P. Fulay, Wendelin J. Wright, The science and engineering of materials., 2010.

[46] R.F. Li, Z.S. Yu, K. Qi, F.M. Zhou, M.F. Wu, C. Yu, Growth mechanisms of interfacial compounds in arc brazed galvanised steel joints with Cu97Si3 filler, Mater. Sci. Technol. 21 (2005) 483–487. https://doi.org/10.1179/174328405X29294.

[47] Z.S. Yu, R.F. Li, K. Qi, Growth behavior of interfacial compounds in galvanized steel joints with CuSi3 filler under arc brazing, Trans. Nonferrous Met. Soc. China (English Ed. 16 (2006) 1391–1396. https://doi.org/10.1016/S1003-6326(07)60026-0.

[48] H.L. Lin, C.H. Lee, H.Y. Chen, F.J. Nan, Effects of the MIG weld-brazing parameter on the lap-joint performance of aluminum alloy to galvanized steel sheet, Proc. 2018 IEEE Int. Conf. Adv. Manuf. ICAM 2018. (2019) 40–43. https://doi.org/10.1109/AMCON.2018.8615082.

[49] T.T. Ngo, C.C. Wang, J.H. Huang, V.T. Than, Estimating heat generation and welding temperature for gas metal arc welding process, Appl. Therm. Eng. 160 (2019) 114056. https://doi.org/10.1016/j.applthermaleng.2019.114056.

[50] M. Shehryar Khan, Y.H. Cho, M. Alfano, F. Goodwin, E. Biro, Y. Zhou, A systematic

study on the effect of coating type and surface preparation on the wettability of Si-Bronze brazing filler material on GI and GA-coated DP600, Surf. Coatings Technol. 425 (2021) 127735. https://doi.org/10.1016/j.surfcoat.2021.127735.

[51] F. Varol, E. Ferik, U. Ozsarac, S. Aslanlar, Influence of current intensity and heat input in Metal Inert Gas-brazed joints of TRIP 800 thin zinc coated steel plates, Mater. Des. 52 (2013) 1099–1105. https://doi.org/10.1016/j.matdes.2013.06.054.

[52] F. Varol, Investigation of mechanical properties of MIG-brazed 304 stainless steel and en 10292 galvanized steel joints using different current intensity, Acta Phys. Pol. A. 131 (2017) 34–35. https://doi.org/10.12693/APhysPolA.131.34.

[53] P. Makwana, M. Shome, S.F. Goecke, A. De, Wetting length in gas metal arc brazing of galvanised steel, Sci. Technol. Weld. Join. 22 (2017) 166–169. https://doi.org/10.1080/13621718.2016.1207289.

[54] R.E. Goland M, The stresses in cemented joints, J. Appl. Mech. 11 (1994) A17.

[55] X. Zhao, R.D. Adams, L.F.M. da Silva, A new method for the determination of bending moments in single lap joints, Int. J. Adhes. Adhes. 30 (2010) 63–71. https://doi.org/10.1016/j.ijadhadh.2009.09.001.

[56] D.W. Oplinger, Effects of adherend deflections in single lap joints, Int. J. Solids Struct. 31 (1994) 2565–2587. https://doi.org/10.1016/0020-7683(94)90037-X.

[57] Y.H. Cho, M. Shehryar Khan, F.E. Goodwin, Y.N. Zhou, Effect of torch angle and position on bead geometry and joint strength during arc brazing of thin-gauge dual-phase steel, Int. J. Adv. Manuf. Technol. (2022). https://doi.org/10.1007/s00170-022-09309-7.

[58] H. Ma, G. Qin, X. Bai, L. Wang, Z. Liang, Effect of initial temperature on joint of aluminum alloy to galvanized steel welded by MIG arc brazing-fusion welding process, Int. J. Adv. Manuf. Technol. 86 (2016) 3135–3143. https://doi.org/10.1007/s00170-016-8425-7.

[59] A. Koltsov, N. Bailly, L. Cretteur, Wetting and laser brazing of Zn-coated steel products by Cu-Si filler metal, J. Mater. Sci. 45 (2010) 2118–2125. https://doi.org/10.1007/s10853-009-3949-y.

[60] W. Reimann, S. Pfriem, T. Hammer, D. Päthe, M. Ungers, K. Dilger, Influence of different zinc coatings on laser brazing of galvanized steel, J. Mater. Process. Technol. 239 (2017) 75–82. https://doi.org/10.1016/j.jmatprotec.2016.08.004.

[61] R. Cao, J.H. Chang, Q. Huang, X.B. Zhang, Y.J. Yan, J.H. Chen, Behaviors and effects of Zn coating on welding-brazing process of Al-Steel and Mg-steel dissimilar metals, J. Manuf. Process. 31 (2018) 674–688. https://doi.org/10.1016/j.jmapro.2018.01.001.

[62] ASTM E8, ASTM E8/E8M standard test methods for tension testing of metallic materials 1, Annu. B. ASTM Stand. 4. (2010) 1–27. https://doi.org/10.1520/E0008.

[63] E.B.F. Dos Santos, L.H. Kuroiwa, A.F.C. Ferreira, R. Pistor, A.P. Gerlich, On the visualization of gas metal arc welding plasma and the relationship between arc length and voltage, Appl. Sci. 7 (2017). https://doi.org/10.3390/app7050503.

[64] J.C. Amson, Lorentz force in the molten tip of an arc electrode, Br. J. Appl. Phys. 16 (1965) 1169–1179. https://doi.org/10.1088/0508-3443/16/8/316.

[65] A.O. Cynthia L. Jenney, Welding Handbook, Vol. 1, 9th ed., Woodhead publishing Ltd; 9th edition, 2001. https://doi.org/10.1007/978-1-349-00324-2.

[66] J. Hu, H.L. Tsai, Heat and mass transfer in gas metal arc welding. Part I: The arc, Int. J. Heat Mass Transf. 50 (2007) 833–846. https://doi.org/10.1016/j.ijheatmasstransfer.2006.08.025.

[67] M. Pouranvari, Effect of resistance spot welding parameters on the HAZ softening of DP980 ferrite-martensite dual phase steel welds, World Appl. Sci. J. 15 (2011) 1454–1458.

[68] H. Bhadeshia, R. Honeycombe, Iron-Carbon Equilibrium and Plain Carbon Steels,

2017. https://doi.org/10.1016/b978-0-08-100270-4.00003-2.

[69] S. Kou, Welding Metallurgy, 2nd ed., John Wiley and Sons, Hoboken, NJ, 2003. https://doi.org/10.22486/iwj.v4i3.150243.

[70] M. Kai, Y. Zhishui, Z. Peilei, L. Yunlong, Y. Hua, L. Chonggui, L. Xiaopeng, Influence of wire feeding speed on laser brazing zinc-coated steel with Cu-based filler metal, Int. J. Adv. Manuf. Technol. 76 (2014) 1333–1342. https://doi.org/10.1007/s00170-014-6347-9.

[71] M. Shehryar Khan, Y.-H. Cho, M. Alfano, F. Goodwin, E. Biro, Y. Zhou, A systematic study on the effect of coating type and surface preparation on the wettability of Si-Bronze brazing filler material on GI and GA-coated DP600, 2021.

[72] A.J. Kulkarni, K. Krishnamurthy, S.P. Deshmukh, R.S. Mishra, Effect of particle size distribution on strength of precipitation-hardened alloys, J. Mater. Res. 19 (2004) 2765–2773. https://doi.org/10.1557/JMR.2004.0364.

[73] Y.H. Cho, M.S. Khan, A.R.H. Midawi, S. Zhang, F. Goodwin, Y.N. Zhou, Effect of gap clearance on the mechanical properties of GMA-brazed lap joint, Manuf. Lett. (n.d.) Under review.

[74] W.D. Pilkey, D.F. Pilkey, Shoulder Fillets, in: Peterson's Stress Conc. Factors, Second, John Wiley & Sons, Inc., Hoboken, NJ, USA, 2008: pp. 135–175. https://doi.org/10.1002/9780470211106.ch3.

[75] Y.H. Cho, M. Shehryar Khan, F.E. Goodwin, Y.N. Zhou, Effect of torch angle and position on bead geometry and joint strength during arc- brazing of DP600, Int. J. Adv. Manuf. Technol. (2022).

[76] D.F. O'Kane, K.L. Mittal, Plasma Cleaning of Metal Surfaces, J Vac Sci Technol. 11 (1974) 567–569. https://doi.org/10.1116/1.1318069.

[77] W. Reimann, M. Dobler, M. Goede, M. Schmidt, K. Dilger, Three-beam laser brazing of zinc-coated steel, Int. J. Adv. Manuf. Technol. 90 (2017) 317–328.

https://doi.org/10.1007/s00170-016-9361-2.

[78] M. Shehryar Khan, Y.H. Cho, S. Zhang, F. Goodwin, E. Biro, Y. Zhou, The effect of zinc coating type on the morphology, joint geometry, and mechanical properties of Si-Bronze arc brazed thin-gauge automotive steel for the journal, Metall. Mater. Trans A - Under Rev. (n.d.).

[79] J. Freudenberger, H. Warlimont, Copper and C 293 12. Copper and Copper Alloys, (2018) 293–301. https://doi.org/10.1007/978-3-319-69743-7_12.

Appendices

Appendix A

Average result of bead geometry measurements.

Torch position and angles				Bead geometry measurements							
Sample#	TP (mm)	Work (α°)	Push (β°)	W (mm)	H (mm)	L_1 (mm)	L_2 (mm)	S (mm)	θ (°)	PMZ_1 (mm^2)	PMZ_2 (mm^2)
1	1	10	0	4.98	2.23	4.25	4.37	1.55	56	0.34	0.16
2	-1	10	0	4.50	3.34	0.64	1.32	0.98	127	1.03	0.00
3	1	10	30	5.37	2.00	4.14	4.77	1.33	55	0.17	0.24
4	-1	10	30	6.38	2.33	3.14	3.59	1.66	72	0.91	0.00
5	1	40	0	5.81	1.85	4.70	5.28	1.47	45	0.06	0.17
6	-1	40	0	5.06	2.46	2.56	2.67	2.05	83	0.54	0.00
7	1	40	30	5.03	2.39	3.83	4.44	1.26	39	0.04	0.42
8	-1	40	30	5.28	2.67	0.98	1.32	0.64	74	1.47	0.00
9	1	25	10	5.27	2.22	3.93	4.53	1.22	45	0.20	0.43
10	-1	25	10	4.85	2.44	2.25	2.97	1.84	110	0.85	0.00
11	0	10	0	4.98	2.48	2.95	3.56	1.81	83	0.59	0.02
12	0	10	10	5.27	2.14	3.47	3.72	1.77	67	0.58	0.23
13	0	10	20	5.04	2.23	3.37	3.55	1.67	61	0.39	0.15
14	0	10	30	5.54	2.19	3.66	4.22	1.61	62	0.50	0.21
15	0	25	0	5.32	2.40	3.29	3.71	1.77	60	0.42	0.04
16	0	25	10	5.01	2.21	3.21	3.58	1.71	61	0.43	0.21
17	0	25	20	4.88	2.35	3.39	4.03	1.40	53	0.33	0.19
18	0	25	30	5.52	2.22	3.70	4.36	1.47	40	0.33	0.33
19	0	40	0	5.31	2.09	3.60	4.14	1.66	58	0.30	0.15
20	0	40	10	5.11	2.31	3.75	4.37	1.48	49	0.14	0.17
21	0	40	20	5.59	2.22	3.95	4.35	1.41	51	0.27	0.10
22	0	40	30	5.59	2.10	3.89	4.39	1.41	48	0.28	0.17

Appendix B

Average result of mechanical responses from tensile testing.

Torch position and angles				Mechanical responses	
Sample#	TP (mm)	Work (α°)	Push (β°)	UTS (MPa)	Fracture mode
1	1	10	0	355	BB
2	-1	10	0	91	IF
3	1	10	30	496	BB
4	-1	10	30	319	BB
5	1	40	0	252	BB
6	-1	40	0	378	IF/BB
7	1	40	30	560	BB
8	-1	40	30	125	IF
9	1	25	10	575	HAZ
10	-1	25	10	431	IF/BB
11	0	10	0	455	IF
12	0	10	10	555	BB
13	0	10	20	593	BM/BB
14	0	10	30	568	HAZ/BB
15	0	25	0	527	IF/BB
16	0	25	10	585	BM
17	0	25	20	585	BM/HAZ
18	0	25	30	588	HAZ
19	0	40	0	586	BB
20	0	40	10	561	BM/BB
21	0	40	20	587	BM/HAZ
22	0	40	30	580	BM/HAZ